2021-08-07

IONOSPHERIC RESPONSE TO CME AND CIR DRIVEN GEOMAGNETIC STORM OVER ETHIOPIA FROM 2013-2017

Wubet, Chernet

IONOSPHERIC RESPONSE TO CME AND CIR DRIVEN GEOMAGNETIC STORM OVER ETHIOPIA FROM 2013-2017

A THESIS SUMMITED TO THE SCHOOL OF POST GRADUATE STUDIES,

BAHIR DAR UNIVERSITY, THE DEPARTMENT OF PHYSICS

IN PARITIAL FULFILLMENTMENT OF THE REQUIERMENT

FOR DEGREE OF MASTER SCIENCE IN PHYSICS

BY

Chernet Wubet

Advisor: Ambelu Tebabal (PhD))

BAHIR DAR, ETHIOPIA

Ju1y, 2021

Certification

The undersigned hereby certify that we have read and recommend to the school of postgraduate studies for the acceptance of this thesis work entitled: **IONOSPHERIC RESPONSE DUE TO CME AND CIR DRIVEN GEOMAGNETIC STORM OVER ETHIOPIA FROM 2013-2017** by **Chernet wubet** in Partial Fulfillment of the Requirements for the Degree of **MASTER OF SCIENCE IN PHYSICS** at Bahir Dar University.

Approved By:

_____

Ambelu Tebabal(PhD)

_____

External Examiner

_____

Internal Examiner I

_____

Internal Examiner II

Authorization to Copy

Chernet Wubet hereby authorize the Bahir Dar University to copy and/or release the whole, part of this research work to other researchers and organizations wishing to use the material for reference and/or research purposes.

_____

Dedication

This work is dedicated to my mother and brother for their never-ending love; I have no word to express my love!

Acknowledgments

.

First and for most I would like to thank Bahir Dar University for offering me the opportunity to study MSc degree program. Then I would like to give more thanks to my advisor Dr. Ambelu Tebabal for his encouragement, guidance, comment and advices during my graduate school carrier. I greatly appreciate him for his constant support, encouragement and friendly relation with me over the past my working time. Even though he is very busy of many works, but he has been providing me continous encouragement, and showed me comments and feedbacks. .

Then my deepest gratitude to Dr.Tsegaye, Dr.Melssew, Mr.Geletaw, Mr.Balew and Mr.Mogess for their supporting, encouragement, and advice.

My strongest thank is addressed to my families, especially my beloved mother, brother, and sisters respectively, and I haven't words to thank my beloved, mother and brother, whom have inspired and helped me never-ending financial, and moral support and encouragement throughout my academic carrier, so all of them are the hero of my success, without their encouragement and support, this stage is unthinkable. I would like to thank also all physics department staffs, my lovely classmates,those whom graduated in 2012, 2013.

Chernet Wubet

Table of Contents

List of Tables

List of Figures

List of symbol

Symbol	Meaning
E	Electric field.
B	Magnetic field.
V	Drift velocity.
ω_s	Angular velocity.
θ_s	Latitude in dgree.
T_s	Syndonic rotational period.
K	Normalization constant.
R_z	Sunspot number.
g	Sunspot gruoup.
n	refractive index.
c	Speed of light.
n_p	index of refraction of phase signal.
n_g	index of refraction of group signal.
V_g	Velocity of refraction of group signal.

Acronyms

Acronyms	Meaning
ACE	Advanced Composition Explorer
CIR	Co-rotating Interaction Region
CME	Coronal Mass Ejection
COSMIC	Constellation Observation System for Meteorology, Ionosphere and Climate
DDEF	Disturbance Dynamo-Electric Field
Dst	Disturbed time index
EIA	Equatorial Ionization Anomally
EUV	Exterem Ultra-Violet
FS	Forward shock
GNSS	Global Navigation Satellite system
HF	High frequency
GPS	Global Positioning System
HSSW	High Speed Solar Wind
IF	Interface
IMF	Interplanetary Magnetic Field
LASCO	Large Angle and Spectrometric Coronagraphs
PPEF	Propet Penetration Electric Field
RINEX	Receiver INdependent EXchange
SID	Sudden Ionospheric Disturbance
OSO-7	Seventh Orbiting Solar Observatory
SOHO	Solar and Heilospheric Observatory
TAD	Travelling Atmospheric Disturbance
TEC	Total Electron Content
VTEC	Vertical Total Electron Content

Abstract

In this paper, we present the responses of the ionospheric total electron content (TEC) to coronal mass ejection (CME), and co-rotating interaction region (CIR) driven storms using stations that lie 37°E-39°E geographic longtude in low latitude region from 2013-2017. CME driven geomagnetic storm generally characterised by strong magnetic field, low proton temperature, enhanced solar wind speed and short recovery phase, while CIR driven storm have been characterised by weak magnetic field, high temperature and long recovery phase as compared with CME driven storm. Disturbance time index(Dst_{min} <-88nT) were considered for this study. In this study three CIR and seven CME driven geomagnetic storm has been selected with available TEC data over the selected year and GPS station. TEC data used in this study was derived from the Global Navigation Satellite System observations in RINEX format, that processed by Gps-Gopi soft ware, and ploted by matlab program by importing the file. Statistical analysis of ionospheric storm effect were computed over the selected GPS station by computing VTEC deviation from quiet day monthly running median of VTEC. The number of CIR driven storm is more dominant during the decline phase of the solar cycle period. The number of CME is maximum during March equinox and June solistic.

Our analysis had been shown positive ionospheric response is more prolonged during the recovery for CIR driven storm in the evenning and non significant response during the main phase. Positive ionospheric response highly observed during the main and recovery phase of CME driven driven storm. On low latitude, most positive response obserbed before sunrise at around the midnight due to higher order of ionospheric irregularity.

key Word:Geomagnetic storm,Coronal Mass Ejection, Corotating Interaction Region

Chapter 1

Introduction

1.1 Background of the Study

Sun is the main source of space weather and the ultimate source of energy for the solar system, as it releases energy continuously in the form of electromagnetic radiation, charged particles and magnetic fields which are responsible for the formation and dynamics of the Earths ionosphere and magnetosphere. The weather condition that we observed on the solar system is said to be space weather. It is a branch of space physics, which concerned with the weather conditions in the solar system, that are driven by variable solar activity like Coronal Mass Ejection (CME), Co-rotating Interaction Region (CIR), Solar Flare, SunSpot, and Solar Wind (Patel et al., 2019; Matamba and Habarulema., 2018). Geomagnetic storms, ionospheric disturbances, scintillation, aurora and geomagnetic induced currents are some of the physical phenomena that affect space weather due to the activity of the Sun-Earth interaction (Dugassa et al., 2020b). It is a new field in science today and has very interesting effects on human life, the environment, and technology. Now days scientists are more interested to study space weather with a wide range of tools to try to learn more about the physical and chemical processes that takes place in the upper atmosphere of the ionosphere. One of these tools is Global Positioning System (GPS), which is currently the most popular global satellite positioning systems due to the global availability of signals. GPS satellite designed to orbit the earth at around 20,200 km (Yaacob., 2010).

Ground based stations like GPS, Global Navigation Satelite System (GNSS), and satellite applications are built and launched around the globe to investigate the variability of the ionosphere. The region of the Earth's upper atmosphere where ions and electrons sufficiently concentrated to affect radio wave propagation is ionosphere. It extends from 60km -1000km in altitude (Twino-

mugisha et al., 2017). It is a partially ionized gas that consists of a mixture of charged and neutral particles. Based on height profile as well as particle (ion and electron) composition and particle density, the layer of the ionosphere can be categorized in to three (Brekke., 2013). These are D, E, and F-region.

D-region is the lower ionosphere of the upper atmospher where more dense atoms or molecules are concentrated due to gravitational atraction force that lies below 90km in altitude. It is a very weakly ionized and highly collisional layer (Balasis et al., 2019). The earliest detected layer was the E (90-150) km-layer, so named because of the reflection of electric fields. It ionization peak at about 110 km and above this region is F(>150km)-region that splits in to F1 and F2 layer during the day time, and highly ionized at around 200 km and 300 km altitude respectively. The charged particles in the ionosphere are generated by the process of photo-ionization, and impact ionization (Oryema., 2015). The particles in the ionosphere are ionized by solar radiation which

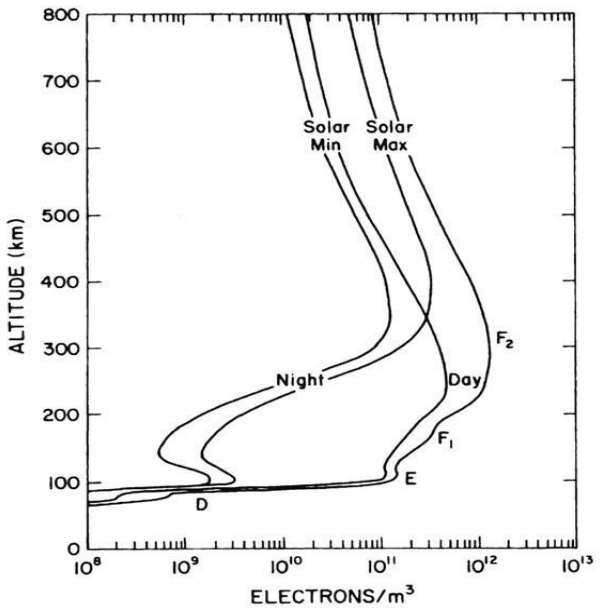

Figure 1.1: Mid-latitude ionospheric electron density profiles for sunspot maximum and minimum conditions at daytime and night-time (Brekke., 2013).

radiates from the sun (solar atmosphere) in to interplanetary space. The energy released from the

sun in to the interplanetary space disturbs the particle in the ionosphere and moves towards the Earth magnetosphere. So that, the interaction of disturbed solar wind which, emanates from the Sun outer surface (corona) in to the Earths magnetosphere, may induce changes in the magnetosphere called geomagnetic storms (Gonzalez et al., 1994). A geomagnetic storm is a worldwide disturbance of the Earths magnetic field, that is driven by variable solar activities like CME, CIR, Solar flare, and Solar wind. The largest storms associated with CME were a huge amount of energetic plasma particles burst (expulsions) out in to the interplanetary space (Chakrabort et al., 2015).

When the polarization of IMF Bz changes from northward to southward, and remains southward for more than three hours and reconnects with the Earths magnetic field. The strong magnetic field and charged particle interact with the earth magnetic field to create a disturbance on the magnetosphere, and ionosphere. The ionospheric storm effects in the equatorial latitude are due to the modification of equatorial ionization anomaly (EIA) by electric fields and winds, neutral composition changes, and wind-induced transport(Yokoyama and Kamide, 1997).

During the geomagnetic storm rapid changes takes place in the global thermosphere and ionosphere following the onset of geomagnetic storms. High latitude thermosphere gets heate and expands to creates equatorward neutral winds and traveling atmospheric disturbances (TAD) that changes thermospheric composition. High latitude ionospheric electric fields penetrate to low latitudes and sub auroral electric fields intensify and expand towards the equator that leads to develope a disturbance dynamo electric field. The changes in the thermosphere and ionospheric electric fields produce rapid, and sometimes dramatic changes in the ionospheric density are called ionospheric storms (VijayaLekshmi et al., 2011). These storm affects our daily life by different ways like an interruption of the communication, affecting navigation, and technology, desturbing the weather condition etc.

These storms can leads unexpected dramatic change in electron density of the F region ionosphere(Chakrabort et al., 2015). During the geomagnetic storms, ionospheric peak electron density (Nmax), electron density (Ne) and TEC increase or decrease dramatically from their normal level, known as positive or negative ionospheric storms respectively. The daytime positive

ionospheric storm effects over the low, equatorial, and middle-latitude ionosphere have been reported due to prompt penetration electric field (PPEF). It is highly variable in magnitude for each storm during daytime mainly causes enhanced eastward electric field leading to strong upward ExB drift, which mainly results in large enhancement in ionospheric TEC, (1TECU = 10^{16} electrons/m^2. PPEF enhances the TEC during day-time sectors and deplete during the night-time. The night time ionospheric storm effects at low latitude could be due to eastward dynamo disturbance electric field (DDEF) that characterize dawn and dusk behaviors (depressed in TEC). Positive ionospheric storms at low and equatorial latitude have been attributed due to neutral composition changes(Prolss and Bonn., 1993). Positive ionospheric storms can cause many serious problems such as time delay, range error, and scintillation in satellite communication and navigation whereas, negative ionospheric storms can cause radio blackouts in the ground-based HF radio communication (Purohit et al., 2015). Since every geomagnetic storm has its unique character and therefore prediction, and forecasting of the response of ionosphere during geomagnetic storms is an interesting topic.

The dependence of the ionospheric response to the CIR-driven geomagnetic activity on altitude, local time, and latitude has also been investigated using different observations. For example, Chen et al. (2015) analized the 9 day oscillations of ionospheric electron densities from the observations COSMIC by using the Kp-index. They suggested that the day time electron density response to recurrent geomagnetic activity is strongly depends on altitude.

1.2 Motivation

Several ground-based and space-based systems are adversely affected by geomagnetic storms. Understanding how geomagnetic storm affects the ionosphere is essential to mitigate their adverse effects on the ground as well on the space. In line with this, researchers have been investigating the ionospheric response of CMEs and CIRs driven storms in several sector. For example, Fagundes et al. (20156) studied the F-region ionospheric response in the Brazil during an extreme space weather event on 17 March 2015 using a large network of 102 GPS-TEC stations. They

analized that VTEC was haighly disturbed during the main and recovery phases.

Dugassa et al. (2020b) studied the ionospheric response to CIR-driven geomagnetic storms across equatorial and low-latitude region of different longitudal sectors. They analized a significant night time positive ionospheric storm observed during the main phase of the storm. Sulungu and Uiso. (2019) studied the occurance of ionospheric response to geomagnetic storms occurred on 15-20 March 2013, and 2015 over the East Africa region. They analized that the main phase of march 17, 2015 were more intense than that of march 17,2013. Adeniyi et al. (1986) examined the effects of geomagnetic storms over F2 region. They analized either positive or non-significant ionospheric response observed during the main and early phases of the recovery phase. According to thier result most of the positive ionospheric storm effects were observed during the March equinox period and the least during June solstices related to high and low solar activity.

Chen et al. (2015) analyzed the response of ionospheric peak electron density of geomagnetic storms by using ionosonde data from 1946 - 1955. They revealed that on average, the ionosphere had a short positive response after the storm onset, followed by highly negative response at high and middle latitudes, where as at low latitude the storm response was mostly positive. Matamba and Habarulema. (2018) investigated TEC response to CMEs and CIRs in middle, low, and equatorial latitudes over the African sector from 2011 to 2015 using stations between 30^0E and 40^0E geographic longitude. They saw the ionospheric variability of ethiopia by using a single GPS station (Nazret). However, the variations of ionospheric responses to geomagnetic activity significantly vary with latitude, longtude and season. Using a multi-GPS station is more essential to show the TEC variablity on the ionosphere than the single GPS station. Due to this both quiet day variability and magnetic storm effects with a multi-GPS station needs more investigation. Therefore the aim of this study was investigating the ionosphere response of CIR and CME by adding a few GPS station TEC data . Understanding the effect of ionospheric response with multi GPS station during quiet and disturbed condition is quite important for effective prediction, forcasting, and signal transmission.

1.3 Objectives

1.3.1 General Objective

The overall objective of this thesis is to investigate the ionospheric response of CME and CIR driven geomagnetic storm over the selected GPS station from 2013 - 2017 through observational and statistical analysis.

1.3.2 Specific bjectives

The specific objectives of this study is to:-

- investigate the diurnal variability of TEC during CME and CIR geomagnetic storm periods.
- compare and contrast CME and CIR geomagnetic storm effect on TEC variability.
- quantified the ionospheric activity indices during the selected CME and CIR geomagnetic storm events .

1.3.3 Significance of the Study

The sources of geomagnetic storms may be divided into two categories based on their solar wind drivers namely, CME and CIR. The CME-driven storms are the main source of transient inter-planetary disturbances such as shock waves may cause problems for the Earth-based electrical systems like power grids , while CIR-driven storms, on the other hand, have been a problem for space-based assets like satellite, navigation and communication. Therefore, investigating the ionospheric response to CME and CIR driven geomagnetic storm will enable to

- get hands-on practice on how to design an antenna using simple antenna wires to trap radio transmission.

- reduce the interference of radio communication by constructing active as well appropriate antenna.
- minimize the disruption of radio transmissions, damaging satellites and electrical transmission line.
- mitigate the sudden dissipation power grid

Chapter 2

Sun-Earth connection

2.1 Sun

Sun is the main source of space weather and the ultimate source of energy for the solar system. Every living and non-living thing uses its energy for its daily life activities. It release energy continuously in the form of electromagnetic radiation, charged particles, and magnetic fields that are responsible for the formation and dynamics of the Earth ionosphere and magnetosphere (Patel et al., 2019). It is a G-type main-sequence star that are composed from (74% Hydrogen) and (25% Helium) by mass and 1% other trace element like Ar, Kr, Co by fusion reaction. It is comprises 99.86% the mass of the solar system, and 4.83% brighter than the stars in the Milky Way galaxy. The mass of the Sun, $M_{\odot} = 2 \times 10^{30}$ kg with equivalent radius $R_{\odot}$=7.8$\times 10^{10}$ and density ρ= $1.4\times 10^{3} \frac{kg}{m^3}$, acceleration due to gravity $g_{\odot} = 2.7\times 10^{2} \frac{m}{s}$, and escaping velocity, $V_{es} = 2\times 10^{5} \frac{m}{s}$. As well the mean distance from the Sun to the Earth is one astronomical unit (1AU=1.5×10^{11} m) and the distance between the Sun and the Earth is about 215 $R_{\odot}$. Since the speed of light (c) is close to $3 \times 10^{8} \frac{m}{s}$, it will take light about 500 seconds or close to 8 minutes to pass from the Sun to the Earth's surface (Brekke., 2013). The temperature at the solar center is assumed to be as high as $1.5 \times 10^{7} K$. The high temperature of its interior and the consequent thermonuclear reactions keep the entire sun to be gaseous (Bittencourt., 2013). At high-temperature proton will be converted to helium nuclei by thermonuclear fusion reactions such as the proton-proton chain. The nuclear burning of proton-proton or pp chain can be illustrated as:

$$ {}_{1}^{1}H + {}_{1}^{1}H \rightarrow {}_{1}^{2}H + e^{+} + v + 0.42MeV $$

$$ {}_{1}^{1}H + {}_{1}^{2}He \rightarrow {}_{1}^{3}He + \gamma + 5.58MeV $$

$$^{3}_{1}He +^{3}_{1} He \rightarrow^{4}_{1} He + 2^{1}_{1}H + 12.8MeV$$

Where, e^{+}, υ and γ represent a positron, a neutrino, and gamma -ray of quantum particle respectively (Brekke., 2013).

The Sun has an important role in helping us to understand the rest of the astronomical universe. It is the only star close enough to us that reveal details about its surface. With out the Sun life did not exist everywhere. It is the main source of energy for the solar system, and the key to understand other stars. It has an interior and exterior region. The Sun's interior region is the core where energy is generated by fusion reaction and diffuses through the radiative zone by the process of photon radiation in the form of X-rays and gamma-rays, and as well through the convection zone by fluid flows (moment of a fluid molecule). Tachocline is the layer found between the radiative and convective zone, which generates a strong magnetic field through electo-dynamo reaction.

As shown in Fig.2.1 the Sun atmosphere is divided into three regions. The closest region to

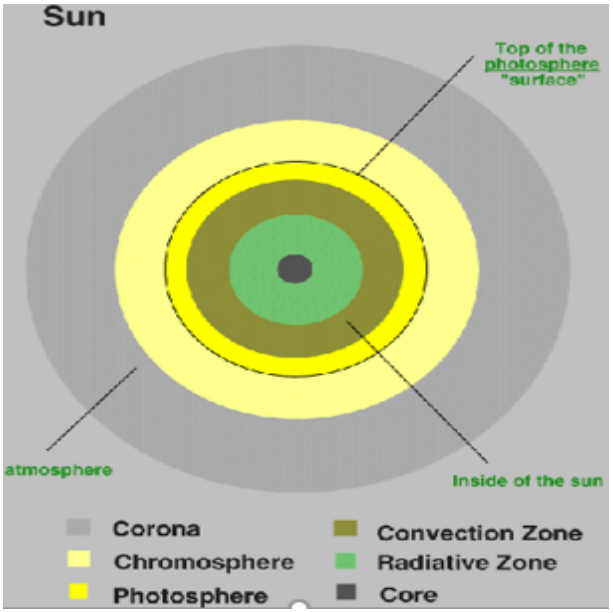

Figure 2.1: Internal and external structure of the sun (http://solar-center.stanford.edu/hidden-pic/photosphere.html).

the inner surface is the photosphere with $10^{23}Nm^{-3}$ in density. It is visible surface of the sun (sphere of light), that extends from the convection zone to the chromosphere. Particle density and temperature decreased as we go out from the bottom to the top of these sphere. By using a simple telescope, a number of features can be observed in the photosphere, like dark regions (sunspots), the bright faculae, and granules. The second region of the solar atmosphere is the chromosphere (reddish color) with $10^{17}Nm^{-3}$ density. Its temperature increase, while its density dicreases as we go out from the bottom. A colorful reddish emission can be seen during total solar eclipses when the moon hides the photosphere (Athay., 2012). The outer layer of the sun with $10^{15}\mathrm{N}m^{-3}$ density, that can be seen during a total solar eclipse as a pearly white crown surrounding the Sun is Corona. Its temperature dramatically increases, while its density decreases as we go out from the bottom to the top part of the corona. The most well-known eruptive process that takes place on the corona is Solar wind, CME, CIR and flare etc. Many physical processes, that takes every where in the universe could be examined through the activity of the sun.

2.2 Solar activites and their effects on Earth

The Sun emits radiation in a wide range of the electromagnetic spectrum from long radio waves to X-rays and other high -energy particles. The basic phenomena that occurred in the solar atmosphere due to the activty of the Sun are solar rotation, Sunspot, Solar Flare, CME, CIR, Aurora and Solar wind etc. Among these some are listed below.

2.2.1 Solar rotation

Every body in the solar system rotates around their axis. Since the Sun is not a completely solid body, its sunspots move from East to West on the solar disk. The rate of movement of sunspots can be used to estimate the rotational period of the Sun. Solar rotation is fastest near the equator and slower at high latitudes. At the equator, the sun rotates approximately once every 25 days and it takes more than 30 days near the poles. The rotational speed of the sun is estimated using Doppler measurements at the solar surface (Imada et al., 2020). Solar differential

rotation can be determined from the positions of the observations of large numbers of magnetic features. The Sun rotates with a synodic angular velocity relative to the Earth, that depends on the heliocentric latitude θ, angular velocity of solar rotation relative to the Earth and Synodic rotation period is given by (Brekke., 2013).

$$\omega_s = 13.4 - 2.7 \sin^2 \theta_s$$

$$T_s = 26.9 + 5.4 \sin^2 \theta_s$$

Where, ω_s is solar angular velocity in degree per day, θ_s is latitude in degree from the equator and T_s is called a synodic rotational period.

2.2.2 Sunspot

A temporary dark spot phenomena observed on the solar photosphere. It can be formed due to strong magnetic field lines deposition (Oryema., 2015).

The strong magnetic field keeps no more heat enters in to these regions and looks dark, because they are much cooler than the surrounding surface of the Sun. The temperature of a big sunspot approximately reaches 3,700^{0}C, where as the temperature of the photosphere reaches around 5,500^{0}C, so that the sun spot appears dark as compared with its surrounding (photosphere). The sun spot consists of two parts. These are the dark area (umbra) which has a strong

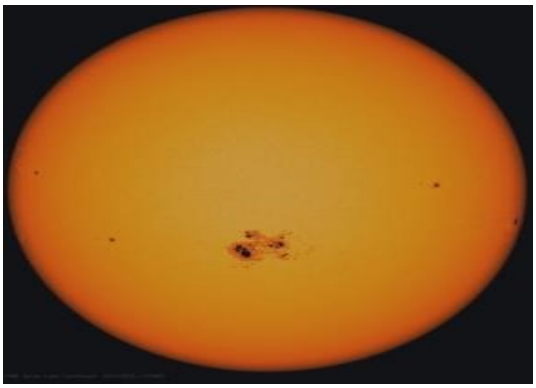

Figure 2.2: Sunspot on the Sun surface captured by SDO on October 23,2014.

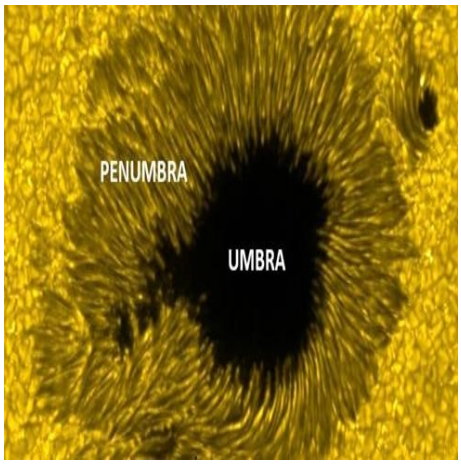

Figure 2.3: Shows umbra and penumbra of sunspot upload from https://www.spaceweatherlive.com/en/help/what-are-sunspot.

vertical magnetic field and the lighter area around the dark (penumbra) that has a weak horizontal magnetic field as compared with umbra as shown in Fig.2.3 (Livingson et al., 2009). Wolf devised a quantitative definition for a sunspot number and studied sun spot data for the years 1700 to 1848 and identified the cycle of the spot, so the average sunspot cycle period takes 11 years. From the Wolf sunspot number R_z is defined as

$$R_z = K(10g + f)$$

Where, R_z is Sunspot number, f is the total number of sunspots regardless of size, g is the number of sunspot groups, and K is a normalization constant accounting for different observatories.

2.2.3 Solar Flare

Solar Flare is a sudden, and rapid release of a huge amount of energy, out from the solar atmosphere with a total power of $10^{20}W - 10^{22}$ W in a very short period of time. It occurs when magnetic energy that has built in the solar atmosphere is suddenly released due to tangling, crossing or reconnection of magnetic fields. It is the out burst of radiation across the electro magnetic

spectrum ranges from radio waves to x-rays and gamma-ray.

(http Space weather Classification of X-ray Solar Flares.html).

The energy released by the solar flare accelerate particles not only downward in the direction of the denser solar atmosphere, but also into interplanetary space along magnetic field lines. The solar flares induce model disturbances to the Earth. The disturbances consists an essential

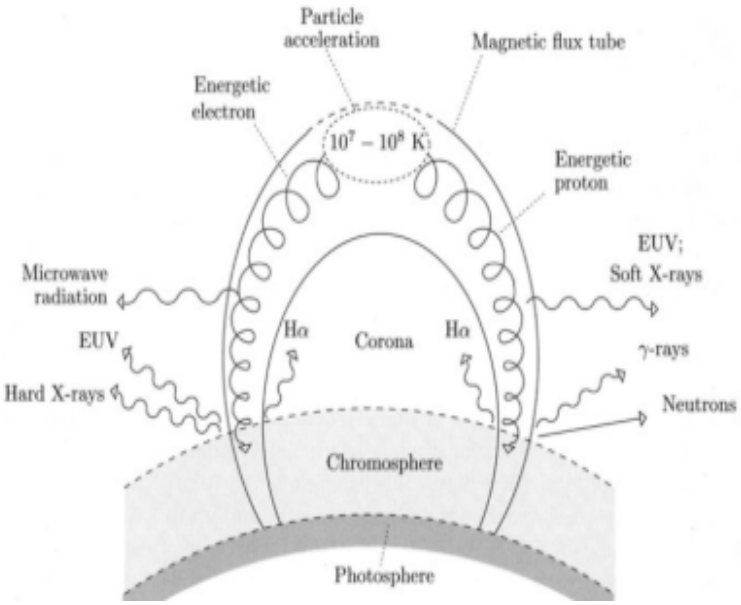

Figure 2.4: Solar flare model, and the possible source of the associated emission (Schillings., 2017).

additional ionization produced by the EUV and X-ray emission, and energetic particles. The rapid increase in the ionization density, sudden ionospheric disturbance (SID) leads to an abrupt change in the reflection conditions for radio waves (Lingerew., 2019). According to their x-ray brightness level solar flares can be grouped in to X, M, C, A, and B class flares within the wavelength range 1 to 8 A^0. X-class flares are big; they are major events that can trigger planet-wide radio black outs and long-lasting radiation storms. M-class flares are medium-sized that can cause radio blackouts, which affect Earth's Polar Regions. C-class flares are small-sized as compared to X and M, and also B and A class flare with decreasing order of its intensity respectively as shown in Table 1.1 (Schillings., 2017).

Each category of flares has nine subdivisions ranging from 1-9, e.g., A1 to A9, B1 to B9

Table 2.1: Solar flare class with its intensity.

Solar Flare Class	Intensity (Wm^{-2})
A	I< 10^{-7}
B	$10^{-7} \leq$ I< 10^{-6}
C	$10^{-6} \leq$ I< 10^{-5}
M	$10^{-5} \leq$ I< 10^{-4}
X	I $\geq 10^{-4}$

continue to X1-X9. The multipliers in each subdivision are used to indicate the level each class. For example,X5 implies $5 \times 10^{-4} Wm^{-2}$.

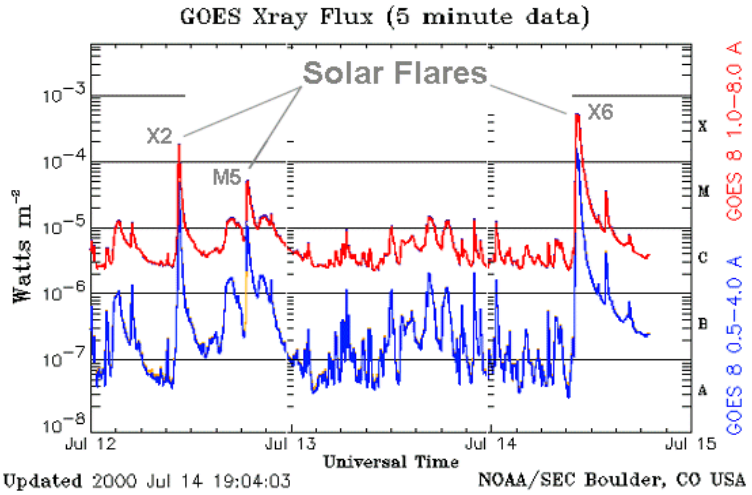

Figure 2.5: Shows a series of solar flares detected by NOAA satellites in July 2000 (http:Space weather Glossary Classification X-ray Solar Flares.html).

2.2.4 Coronal Mass Ejection

The energy emitted from the sun to the earth magnetosphere, thermosphere and ionosphere. The most powerful eruptive phenomenon from the sun is Coronal Mass Ejections (CME). It is the out burst of solar energetic particle out from the active region (Corona, Sunspot) of the Sun in to the interplanetary space that deposits energy, momentum, and magnetic field in to the earth magnetosphere and interplanetary space (Rishbeth et al., 2015). The first CME was discovered in 1971 (Bronarska et al., 2017). Fig.2.6 shows the mass flow of CME out of the active region of

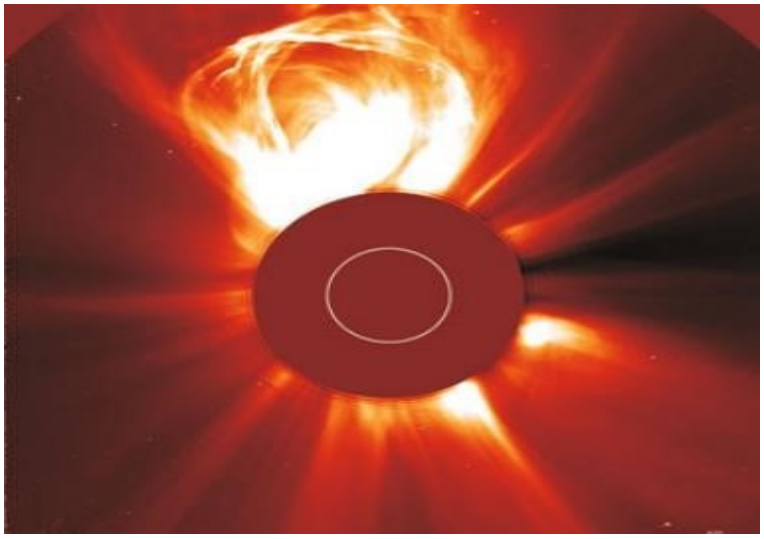

Figure 2.6: Show the Coronal mass ejection of February 27, 2000 as observed by the LASCO instrument aboard the SOHO satellite. NASA/SOHO (Alexander Piel., 2010

the sun in to the interplanetary space. It can be observed during Solar maxima when the activity of the Sun is over the head (Matamba and Habarulema., 2018). The massive stream of solar wind particles transfer an energy and momentum into the magnetosphere. The subsequent interaction cause an intense geomagnetic storms to occur with minimum Dst index ($Dst_{min} < -100$nT). CME-driven geomagnetic storm are generally intense and occur predominantly during the high solar activity periods (Abdu et al., 1997). It is the most dangerous and destructive space weather events that occurred on the interplanetary space (Jin.S and Jin.R., 2017). Since geomagnetic

storm is a worldwide disturbance of the Earth's magnetic field, associated with solar activitie that can be occured when un abnormal south ward energetic magnetic field particle ejected from the Sun and interact with the earth magnetosphere (Patel et al., 2019). Studying the main causes of worldwide disturbances of Earth's magnetic field is important to understand the dynamics of the solar-terrestrial environment of the world.

2.2.4.1 Impact of CME

When the ejection is directed towards the Earth and reconnect, the shock wave of the traveling mass of solar energetic particles causes a geomagnetic storm that may disrupt Earths magnetosphere by compressing it in the day side and stretch in to long tail in the night side, and releases power on the order of tera watt scale, which is directed back toward Earths upper atmosphere. Solar energetic particles can causes strong aurora in large regions around Earths magnetic poles. These are Northern light (aurora borealis) in the northern hemisphere, and the Southern lights (aurora Australias) in the southern hemisphere. CME can disrupt the radio transmission, communication and cause damage to satellites and electrical transmission line facilities, resulting in massive and long-lasting power outages . CME can cause an increase in the number of free electrons in the ionosphere, especially in the high-latitude polar regions. The increase in free electrons can enhance radio wave absorption. Humans at high altitudes, as in airplanes or space stations, risk exposure to relatively intense cosmic rays.

2.2.5 Co-rotating interaction region

The occurrence of the coronal hole on the outer surface of the Sun leads to a high and open magnetic field line (one side attached to the Sun and the other floating in interplanetary space) released high- and low-speed solar plasma streams. Coronal holes at high solar latitudes are larger during solar minimum and eject HSSs, which travel in the interplanetary medium with speeds of (500 - 800)km/s. High-speed structure are emanated by coronal holes and interacts with the low-speed equatorial Streams(300 - 400)km/s creating CIRs which co-rotate with the Sun (Candido et al., 2018). The high oscillatory nature of the IMF-Bz present in these structures

and their positive and negative inversions may cause reconnection with the Earths magnetic field, prompt penetration of interplanetary electric field.

CIR is responsible for the occurrence of weak to moderate geomagnetic activity on the magnetosphere(Candido et al., 2018). The weak and moderate storm is mostly characterized by its minimum Dst index and long recovery phase. The storm caused by CIR is weak (-50nT<Dst_{min} $\leq$-30nT) and moderate (-100 < Dst_{min} $\leq$-50nT) (Liu et al., 2015), and long recovery phase which lasts from a day to many weak. There are two kinds of solar wind that are responsible to create a co-rotating interaction region around the Sun. These are

- **Slow Streams**: They originate above and near the closed magnetic field loops and streamers in the corona at about 400 km/s.
- **Fast Streams**: It originates in the cooler regions of the corona with an Open magnetic field lines with an ($\approx$ 800 km/s) solar wind speed.

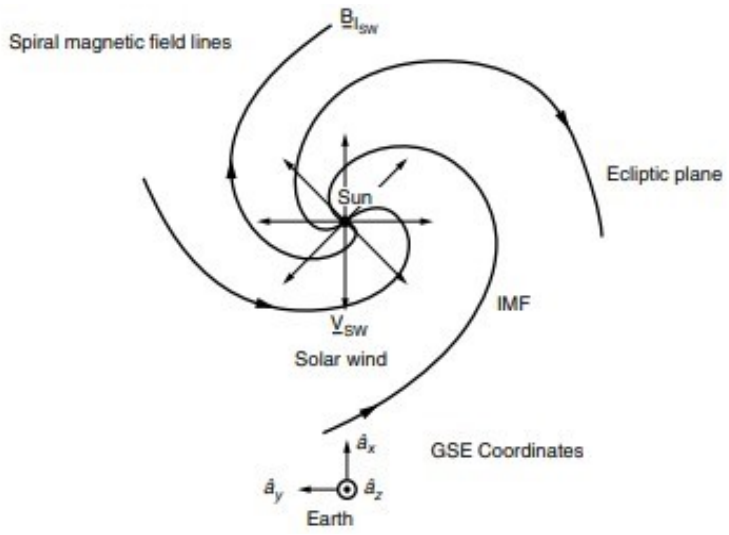

Figure 2.7: The spiral magnetic field as it is stretched out by the solar wind (Kelley., 2013). GSE - Geocentric solar ecliptic

Fig.2.7 indicates the spiral pattern that produced due to a continuous rotation plasma flow. The quiet weak IMF, is about 1 $\times 10^{-5}\beta$ at the surface of the Earth, carried out into interplanetary

space by the solar wind, and travels out in the spiral pattern.

2.2.6 Solar Wind

The environment surrounding the Sun contains a flow of mostly charged particles (electrons, protons and ions), α-particles and smaller amounts of ionized heavier element. The solar wind is a plasma of ionized charged particles blowing out ward from the Sun magnetic field in to all directions at very high speeds (250 - 1000) km/s due to a huge difference in gas pressure (**?**).

2.3 The Earth Ionosphere

The structure and properties of the ionosphere depends on the occurrence of solar activity, variations of Earth's magnetic field, movement of neutral wind in the upper atmosphere due to Earths rotation, the effects of electrical current and ambient electrical fields, density and the content of the atmosphere at different altitudes and geographical latitudes and so on. The existence of an ionized conducting layer in the upper atmosphere was fully proven, when the existence of the ionosphere was demonstrated by studies of the reflections of radio waves from the atmosphere. It is viewed as a variable shell of ionization (plasma) surrounding the Earth. The range variability in vertical profiles of electron density extends around 100 km up to 800 km in altitude (Brekke., 2013).

2.3.1 Ionospheric Region

The region of the upper atmosphere where ions and free electrons are sufficient to affect the frequency of electromagnetic (radio) wave propagation. Its ionization varies depending on the activity of the Sun and cosmic rays that radiate from the comete. The density of molecule varies depending on sunspot cycle, season, altitude and latitude etc.The ionospheric electron density (N) at a given altitude and location depends on the solar EUV fluxes, the neutral composition, dynamical effects of neutral winds, and electric field.

2.3.2 Vertical Profile of the ionosphere

The vertical structure of the ionosphere is changing continuously. It varies from day to night, with the seasons of the year, and with altitude. In terms of altitude, the ionosphere may be divided into three different regions. These are D, E, and F-region are formed by their chemical components and their ability to absorb different wavelengths of radiation emitted from the Sun. Fig.2.8 indicates the hieght profile region of the ionosphere at different altitude range are labeled

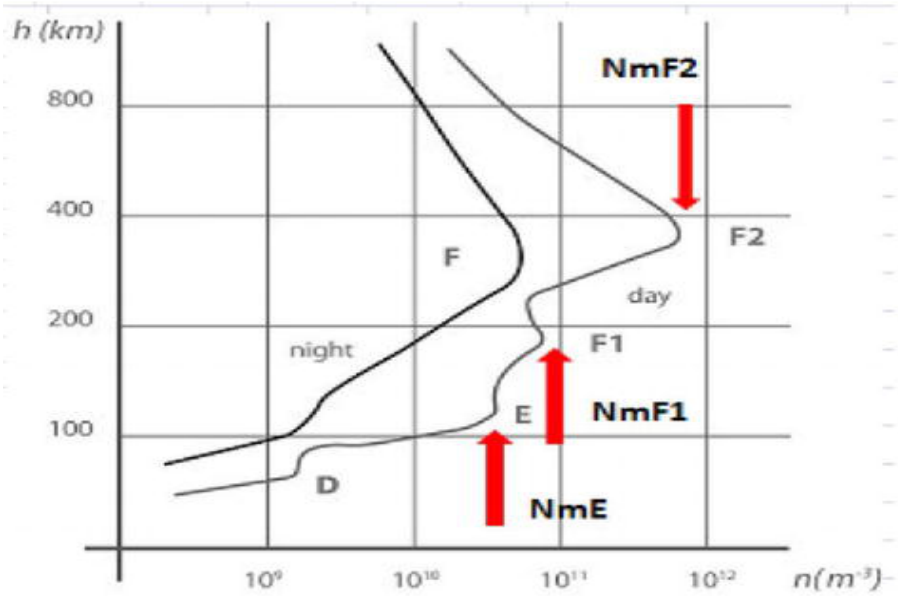

Figure 2.8: Mid-latitude ionospheric electron density profiles for sunspot maximum and minimum conditions at daytime and night-time (Brekke., 2013).

with the appropriate alphabetical order (Brekke., 2013). The earliest detected layer was the E-layer, so named because of the reflections of electric fields at the E-layer. We have D and F-layers below and above the E-layer, respectively (Shim., 2009)

D-layer.

D-region is the lower layer of the ionosphere which extends (60 - 90) km. The radiation within it is only present during the day, and disappeared at night due to recombination of ion. Free ion in the D-region generated by the action of Lyman-α- radiation within the wavelength $1215A^0$

and ionized nitric oxide gas (NO_2) present in the atmosphere. Hard X-ray also contributes to ionize(NO_2, O_2) to wards the peak of the solar cycle and EUV radiation spectrum ionize O_2 molecule with (102.7nm-111.8nm).These region affects radio communication signals particularly in the LF and MF portions of the radio spectru (Brekke., 2013).(https://www.electronics-notes.com/articles/antennas-propagation/ionospheric/ionospheric layers-regions-d-e-f1-f2.php).

E-Layer.

E -region is above the D region that exists in the range altitude (90 - 150) km. E-region air density is very much less than D-region. Free electrons are excited by radio signals and vibrate, far fewer collisions to occur. The electrons are again set in motion by the radio signal, but they tend to re-radiate it. The tendency of "reflection" is dependent upon the frequency and the angle of incidence. As the frequency increases, the amount of refraction decreases until a frequency is reached where the signals pass through the region. Soft X-Rays, and EUV rays used to ionize neutral molecules in E-region with in the wavelengths range (10 -100)A^0. E-region remains at night with a very weak ionized electron density.

F-layer.

The most important region in the ionosphere for long-distance HF radio communications is the F-region. During the day time when radiation is being received from the Sun, it often splits into F_1 and F_2 layer (Farid et al., 2020). The F_1-layer is only observed during the day-time, since the electron densities are primarily controlled by the zenith angle. The main source of ionization in the F_1-layer is the EUV, where its peaks electron density reached $2.5\times10^5 cm^{-3}$ at 210 km with noon time. The F_2-layer is the highest layer in the ionosphere, that have the highest free electron density (Balan et al., 2009). F_2 peak is formed at about 300 km with peak electron density values of $10^6 cm^{-3}$ at noon, and $10^5 cm^{-3}$ at night. Much of the ionization results from ultra-violet light in the middle of the spectrum as well as those portions of the spectrum with very short wavelengths (100-1000)A^o. F1 layer disappeared at night, but not F2. In space-based communications, the F2-layer is the main concern for GPS users due to the absolute ranging errors caused by the larger electron densities in F2-region (Ratnam et al., 2016).https://www.electronics-notes. com/articles/antennas-propagation/ionospheric/

ionosphericlayers-regions-d-e-f1-f2.php.

2.4 Geomagnetic Regions of the Ionosphere

Latitudinal variations of the Earth's ionosphere show distinct behaviors due to the geometry of the Earth's magnetic field lines. Besides the vertical layered profiles of the Earth's ionosphere which includes D, E, and F-region, the ionosphere is also divided into three distinct regions depending on their geomagnetic locations that can be controlled by different physical processes.

2.4.1 The Low-Latitude (Equatorial) Ionosphere

The equatorial ionosphere spans about $\pm 20^0$ on either side of the magnetic equator. The morphology of the equatorial ionosphere is unique and different from mid, and high latitudes because the magnetic field is nearly horizontal to the earth's surface. During the day time, solar heating of the thermosphere drifts ionospheric plasma up ward under the influences of an eastward-directed electrojet electric field and the northward horizontal geomagnetic field. Due to gravity and pressure-gradient forces, the uplifted plasma then moves downward along the magnetic field lines on both sides. The low-latitude ionospheric storms occured due to the modification of equatorial anomaly by electric fields and wind-induced transportation of the neutral composition changes (Matamba and Habarulema., 2018).

2.4.2 Mid-Latitude

The mid-latitude region of the ionosphere includes geomagnetic latitudes about ($\pm 30^0$ - $\pm 60^0$) on either side of the hemisphere. In the mid-latitude region, the photon radiation is responsible for the ionization process and the electron density is generally not affected by the particle radiation. The enhanced upward vertical E$\times$B drifts due to storm time eastward penetration electric field transport plasma to higher altitudes where recombination rate is low. The diffusion of plasma along magnetic field lines can lead to EIA's expansion to lower/middle latitudes and produce an increased TEC. EIA and TID responsible for the enhancement, and neutral composition

changes for the depression (negative affect) of TEC in mid-latitude region (Prolss and Bonn., 1993).

2.4.3 High-latitude region

The polar region is sub-divided in to the aurora zone (approximately $\pm(60^0 - 70^0)$ geomagnetic latitudes) and the polar cap (pole-ward of the aurora zone). At high latitudes the geomagnetic field runs nearly vertical and this leads to the existence of an ionosphere that is considerably more complex than that in the middle and low latitudes. This is because the geomagnetic field lines connect the high latitudes to the outer part of the magnetosphere which is driven by the solar wind.

2.5 Formation of the ionosphere

In this section, we are going to describe briefly how the ionosphere is formed. The grade of ionization depends on the intensity and the wavelength of the incoming radiation, as well as the composition of the atmosphere. Plasma exists in an environment that provides for a large number of ionization processes of atoms. When solar radiation strikes with the dominant electrically neutral species in the upper atmosphere of the Earth, the electrons break the bond of the atom and molecule to produce ionospheric plasma on the day side of the earth when short wave length solar radiation (extreme ultraviolet and X-ray) enough to produce ionization. This mechanism of ion production is photoionization. The other mechanism of ion production occurred when energetic particles penetrate in to the atmosphere collide with the neutral particle. These are said to be Impact ionization.

Photoionization

$$Y + hv \rightarrow Y^+ + e^-$$

Impact ionization

$$X + e^-_{preciptate} \rightarrow X^+ + e^-_{etached} + e^-_{preciptate}$$

Where, Y and X represent neutral atoms or molecules of the atmosphere of the Earth, hυ is the radiate energy from the sun, $e^{-}_{preciptate}$ represents the ionizing energetic particle. The Y^{+} and X^{+} terms represent the ionized atoms or molecules of the ionosphere while e^{-} represents the free electron. Fig.2.9 indicates the ion production mechanism. The ion production depends on

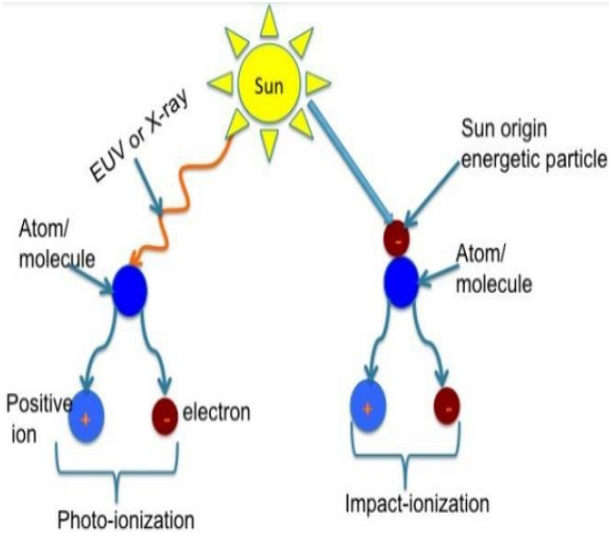

Figure 2.9: Represents the ion production mechanism Nigussie (2013).

the neutral density of atmosphere and radiation intensity from the Sun. Solar irradiation intensity decrease due to absorption as we go down to the Earth's atmosphere where the density increases. Maximum ionization rate q occurs at some altitude where the activity of the sun is over head.

2.6 Variability of the ionosphere

The sun and its activities are the main driver of ionization in the ionosphere. Thus, the ionospheric structure and the electron density distribution vary considerably with time (diurnally and seasonally), geographic location, suns activity (sunspot cycle) and with other solar-related ionospheric and geomagnetic activity (Kelley., 2013).

2.6.1 Diurnal variation

The ionosphere exhibits a diurnal variation. TEC is higher during the day and lower at night. As the Earth rotates with respect to the sun, the intensity of the solar radiation increases, the ionization also increases to a maximum at around noon (overhead Sun), but during in the afternoon, the sun is inclined with a certain angle. The ionization begins to decrease due to electron loss through the recombination and attachment of electron and become very thinner during the night time (Kassa., 2017).

2.6.2 Seasonal Variation

When the Earth revolves around the sun a seasonal cycle is generated determined by which hemisphere the sun is overhead. It is summer in the hemisphere where the sun is overhead and winter in the other hemisphere. For example, December, January, and February are summer for the southern and winter for the northern hemisphere while, June, July, and August is summer for the Northern and winter for the Southern hemisphere. Electron densities are greater in summer than winter in both hemispheres because of the overhead Sun (Vander., 2003). The sun is overhead at the equator around the time of equinoxes. The ionospheric storm effects were grouped in to four seasons, namely, December solstice (November, December, and January), March equinox (February, March, and April), June solstice (May, June, and July), and September equinox (August, September, and October) (Wyllie., 2007)

2.6.3 Solar cycle variation

The 11-year variations in solar activity are important sources of the variations in the solarterrestrial environment. The solar surface rotates differentially in terms of latitude which is called differential rotation. The rotation is fastest near the equator and slower at high latitudes. At the equator, the sun rotates approximately once every 25 days, and it takes more than 30 days near the poles. It is well known that the maximum number of sunspots differs during each 11-year cycle. Some cycles show a large number of sunspots, whereas other cycles show a fewer number

of sunspots. During the maximum number of sunspots, the sun radiates maximum radiation in to the space and maximum ionization is generated and minimum during lower sun-spot number (Imada et al., 2020).

2.7 Ionospheric disturbances

Ionospheric disturbances can result from solar disturbances /or geomagnetic field disturbances. The ionospheric disturbances are associated with the activity of the Sun.

2.7.1 Ionospheric storm

The erupted phenomena like CME, CIR, and Solar flares often produce large variations on the earth magnetosphere and the disturbed earth magnetosphere releases disturbed energetic particle in to the upper atmosphere and generates large disturbance on the ionospheric density distribution, total electron content, and the ionospheric current system is said to be an ionospheric storm.

2.7.2 Geomagnetic storm

The term geomagnetic storm was first used by Chapman and Bartels (1940) to describe the occurance of magnetospheric and ionospheric disturbances (Guarnieri et al., 2006). It is a temporary disturbance of the Earth's magnetosphere caused by a solar wind shock. The frequency of geomagnetic storm is either increase or decrease within sunspot cycle. During solar maximum, geomagnetic storms mostly occurred due to CME driven, but during solar minimum, storms are mainly driven by CIRs (though CME storms are more frequent at solar maximum than at minimum) (Chakrabort et al., 2015). Geomagnetic storm occurs following the polarization of IMF Bz. When the polarization of IMF Bz changes southward and remains southward for several hours and reconnects with the Earths magnetic field (Gonzalez et al., 1994). The erupted solar wind pressure initially compresses the earth magnetosphere and the solar wind magnetic field will interact with the Earth magnetic field and transfer an increased amount of energy and momentum

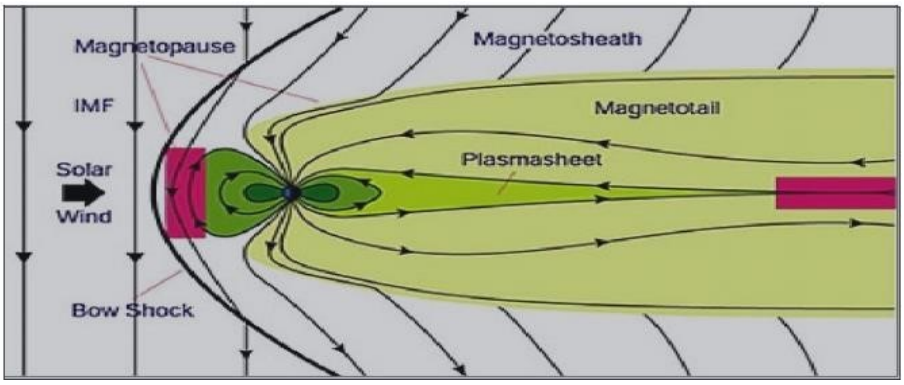

Figure 2.10: An illustration of the large flare associated CME produced geomagnetic storm .

into the magnetosphere (see,Fig.2.10 when the interaction reached in to its maximum limit energetic particles brust out in to the upper atmosphere of the ionosphere. The ionosphere suffers major perturbations during geomagnetic storms which are called ionospheric storms. Ionospheric storms are mainly caused by processes driven from solar phenomena such as CMEs and solar flares, CIR, and Solar wind. The response of the ionosphere to a specific geomagnetic storm depends on the onset time of the magnetic storm, season, solar activity, and the latitude region (Matamba et al., 2015). Geomagnetic storm has typically illustrated by its Dst index. It has three basic phases. These are initial, main and recovery phase (Guarnieri et al., 2006). The initial phase is characterized by Dst (one-minute component SYM-H) increasing by 20nT -50 nT in ten minutes. The initial phase is also referred to as a storm sudden commencement (SSC). However, not all geomagnetic storms have an initial phase and not all sudden increases in Dst. The initial phase is caused by an increased solar wind dynamic pressure acting on the magnetosphere. The increased pressure compresses the dayside magnetosphere, forcing the magnetopause current closer to the Earth, and at the same time increasing it (Kugblenu., 1999). The main phase of a geomagnetic storm is defined by Dst decreasing to less than -50 nT. The selection of -50nT to define a storm is some arbitrary. The minimum value during a storm will be between -50nT and approximately -600nT. The duration of the main phase is typically 2 - 8 hours and recovery phase is occurred when Dst changes from its minimum value to its quiet time. The recovery phase may

last as short as 8 hours or as long as 7 days. Geomagnetic storm activities are usually monitored using geomagnetic storm indices, which includes Dst index, Z-component of the IMF, commonly known as IMF Bz index and Kp-index. VTEC is another parameter that is very essential to study the ionosphere and correlated with Dst.

2.7.3 Disturbed Time Index

The Dst index is an index of magnetic activity derived from a network of near-equatorial geomagnetic observatories that measures the intensity of the globally symmetrical equatorial electro-jet . It is the hourly average component of the magnetic field measured by several ground stations in mid to low latitudes and represents the degree of equatorial magnetic field deviation specifying the Magnitude of Geomagnetic Storms (GMSs) that provided by the World Data Center for Geomagnetism, Kyoto (Borovsky and Shprits., 2017). It describes the variation of the ring current that is used to quantify the strength of the magnetic storm measured in the units of nano Tesla (nT). Based on Dst- index geomagnetic storm grouped into weak, moderate, intense as shown in Fig. 2.11

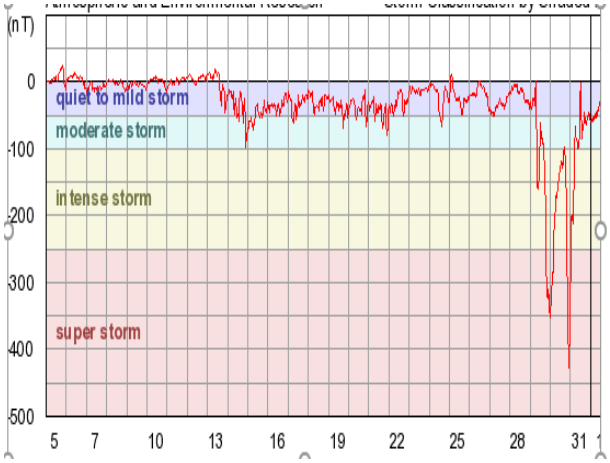

Figure 2.11: A typically profile of Dst index shows geomagnetic storm cassification (Guarnieri et al., 2006).

$$Dst = \frac{1}{N}\sum_{n=1}^{N}\frac{H - H_q}{\cos\phi} \tag{2.1}$$

Where

H-horizontal component magnetic disturbance at given station.

H_q -horizontal component magnetic field of the quietest day.

N-total number of station and ϕ-station latitude.

The $\cos\phi$ factor is to normalized magnetic disturbance at a varius latitudes to the equator

2.7.4 Kp-index

Kp indices give the measure of the biggest disturbance of the Earths magnetic field in periods of three-hour data measurement. Depending on their auroral activities, geomagnetic storms are grouped by using their Kp values. Tabel 2.2 shows the geomagnetic storm classification based on kp values range from 0 - 9.

Table 2.2: Geomagnetic storm calassification.

Kp_index	Go-secale	Auroral activity
0-3	G_O	Quiet
4	G_O	Active
5	G_1	Minor
6	G_2	Moderate
7	G_3	Strong
8	G_4	Sever
9	G_5	Extrem

Tabel 2.2: Shows geomagnetic storm classification based on the previous studies(Huttunen and Schwenn., 2002)

2.7.5 Z-component Magnetic Field(Bz)

The IMF value can be determined by Bz-value and the Bz-value of IMF indicates the total strength of the field i.e, the higher southward value is the better condition for enhanced geomagnetic storm occurred. The IMF is a vector and has three-axis components Bx, By, and Bz. But (Bx and By) are parallel to the elliptic. Due to this, it has no aurora activity effects. Where as Bz is perpendicular to the elliptic and is created by the wave and disturbance on solar wind cause for a geomagnetic storm. Geomagnetic storm occurs when IMF (Bz) turns south-ward direction and interacts with the north-ward direction of the Earths magnetic field. Since the Earth's magnetic field always northward. The two fields attract and interact each other and these causes for the disturbance of geomagnetic storm, this disturbance occurred when the charged particle get easier time to enter the magnetosphere.

2.8 Global Positioning System (GPS)

Space weather is a fairly new field in science today and has very interesting effects on humans, the environment, and technology. It is a wide range of tools to try to learn more about the physics and dynamics that take place in the upper atmosphere. One of these tools is GPS, currently the most popular global satellite positioning system due to the global availability of signals. GPS is a satellite-based navigation radio system that is used to verify the position and time in space and on the Earth (Yaacob., 2010).

The GPS can provide users on a world wide basis with navigation, positioning, and time information. The constellation of navigation satellites operated by the US Department of Defence(DOD) with 24 operational satellites distributed in 6 orbital planes with 4 satellites per plane. The satellites are placed at an altitude of 20, 200 km above the Earth with 12 hrs orbital period and 55^0 orbital inclinations. The time, velocity, and position of GPS satellites are continuously monitored by ground-based network radars (Ratnam et al., 2016). GPS satellites transmit their ephemeris on two carrier frequencies in the L-band for civilian users f1 = 1575.42 MHz (L1) and f2 = 1227.60 MHz (L2). Each GPS signal consists of three components namely carrier,

code, and navigation data. These three components of the signal are derived coherently from one of the atomic standards aboard the satellite. Geomagnetic storms create large disturbances in the ionosphere. The currents and energy introduced by a geomagnetic storm enhance the ionosphere and increase the total height integrated number of ionospheric electrons or the TEC. Near the Earths magnetic equator there are current systems and electric fields that create instabilities in the ionosphere. The instabilities are most severe just after sunset, bubbles, cause GPS signals to scintillate. TEC measurement through GPS is an important tool to study the ionosphere. The ionosphere is a dispersive medium, affects the radio signal propagation that causes a range of errors in GPS communication (Yaacob., 2010). This type of range of error is related to the TEC of the ionosphere. Due to the various increasing application of GPS and to get the higher accuracy in position, a clear understanding of the physical behavior of the TEC is very essential.

2.9 Ionospheric Total Electric Content (TEC)

TEC is the number of electrons present in a ray path between satellite and receiver in the ionosphere. The ionosphere delay radio signal propagation from satellite transmitter to ground receiver, which results in a range measurement error, thus affecting the accuracy of position estimation in satellite-based navigation systems. TEC is used for the computation of the ionospheric delay. An accurate prediction of TEC is helpful to correct the range measurements. TEC varies greatly with the amount of radiation received from the sun. Thus there is a diurnal (time of day) effect and a seasonal effect on the TEC. Radio waves are affected by the presence of electrons. The more electrons in the path of the radio wave, the more the radio signal will be affected. For ground based satellite communication and satellite navigation, TEC is a good parameter to monitor for possible space weather impacts. TEC is measured in electrons per square meter. By convention, 1 TEC Unit (TECU =10^{16} electrons/m). TEC depends on local time, latitude, longitude, season, geomagnetic conditions, solar cycle,and activity. The propagation of radio waves is affected by the ionosphere.

Chapter 3

Data and Methdology

One of the most important parameters to characterize the ionospheric layer is the refraction index. Understanding the index of refraction of the ionosphere is essential when studying the possible propagation effects of ionosphere on the GPS signals. The beam of refraction can be defined by the Snell-Diffraction law. The wave propagation through a medium is characterized by the index of refraction (Markovi., 2015).

$$n = \frac{c}{v} \tag{3.1}$$

Ionosphere is non homogeneous medium. The phase index of refraction at a given location in the ionosphere can be expressed by n_p the Appleton-Hartree formula.

$$n_p = \frac{X}{1 - jZ - \frac{Y_T^2}{2(1-X-jZ)} \pm \sqrt{\frac{Y^4}{4(1-X-jZ)^2} + Y_L^2}} \tag{3.2}$$

$$where, X = \frac{N_e e^2}{\epsilon_o m \omega^2} = \frac{\omega_p^2}{\omega^2}$$

$$Y = \frac{\omega_H}{\omega} = \frac{f_H}{f}.; Y_L = \frac{\omega_L}{\omega} = \frac{f_L}{f}.; Y_T = \frac{\omega_T}{\omega} = \frac{f_T}{f}.$$

$$Y_T = \frac{eB_T}{m\omega} = \frac{\omega_T}{\omega} and Z = \frac{V}{\omega} = \frac{\omega_c}{\omega} = \frac{f_c}{f}; \omega = 2\pi$$

Where f-carrier frequency (Hz).

ω is angular frequency of carrier wave (radian/s).

f_H- gyro frequency of free electron(Hz).

ω_H=$\frac{eB_0}{m}$ - gyro angular frequency of free electron(radian /sec).

ω_L-Longitudinal gyro frequency (radian/s) longitudinal angular gyro frequency, which is calculated according to the formula ω_L=$\frac{eB_o}{m}\cos\theta$.

f_T-Transverse gyro frequency (Hz).

ω_T -Transverse gyro angular freqouency= $\frac{eB_o}{m}\sin\theta$.

f_c-frequency of collisions between electrons and heavy particles(Hz).

ω_c -angular frequency of collisions in (rad/se) and θ–angular freqouency of collision.

f_N-plasma frequency(Hz).

ω_p^2=$\frac{N_e e^2}{\epsilon_o m}$–angular frequency of plasma (radian/s) with N is electron density in electron/m^3.

where, charge of electron (e) is ($1.6\times10^{-19}C$), and dielectric permittivity of free space (ϵ_o) is ($8.8542\times10^{-12}F/m$) and mass of electron(m) is ($9.1095\times10^{31}kg$).

For GPS signals, both the electro-neutral collisions and the effects of the geomagnetic field on the refractive index are negligible Y_T=Y_L=Z=0) at an ultra-high frequency (UHF) of an electromagnetic wave. In such cases the refractive index has only a real part and the estimation of TEC using GPS receivers is made possible by the dispersive nature of the ionosphere (Markovi., 2015). The signal delay caused by TEC in the ionosphere is corrected in the dual-frequency measurement by a linear combination of L_1 and L_2 band frequencies.

$$n_p = 1 - X \tag{3.3}$$

At UHF $X << 1$ due to binomial theorem distribution and elimination the smaller term eq (3.3) can be written as: n_p=1-$\frac{X}{2}$=1-$\frac{N_e e^2}{2\epsilon_o m\omega^2}$ where , ω=2πf and X=$\frac{N_e e^2}{\epsilon_o m\omega^2}$

n_p=1-$\frac{N_e e^2}{8\epsilon_o m\pi^2 f^2}$ $= 1 - \frac{KN_e}{2f^2}$ where, K=$\frac{e^2}{4\epsilon_o m\pi^2}$=80.6 by substituting the value K in the equation the phase index of refraction can be expressed as

$$n_p = 1 - \frac{40.3N}{f^2} \tag{3.4}$$

$$n_g = n_p + f\frac{dn_p}{df} = 1 + \frac{40.3N}{f^2} \tag{3.5}$$

Where n_p and n_g Phase and group refractive index respectivly.

$$\phi_1 = \int Cdt; \phi_2 = \int V_g dt \tag{3.6}$$

$$p = \int V_g dt_{path} \tag{3.7}$$

$V_g = \frac{c}{n_g} = \frac{c}{1 + \frac{40.3N_e}{f^2}}$ for $N_e << f$ then group velocity V_g written as

$$V_g = c(1 - \frac{40.3N_e}{f^2}) \tag{3.8}$$

3.1 Determination of TEC

The ionosphere is a dispersive medium, thus the linear combination of observable on the two frequencies is needed to remove the effect of positioning. On the other hand the dispersive property provides an opportunity to measure directly the ionospheric electron content along the ray path. The equation of motion s=vt where, s-distance in (m), t-time (sec) and v-speed in (m/s). If the motion is in the upper atmosphere,the travel time of an electromagnetic wave through a medium with refractive index n is given by

$$t_{travel} = \int_{raypath} n \frac{dr}{c_{medium}} \tag{3.9}$$

from eq(3.4) $n_p = 1 - \frac{40.3N}{f^2}$ and Eq (3.5) $n_g = 1 + \frac{40.3N}{f^2}$ then the travel time

$$t_{travel} = \frac{1}{c} \int_{raypath} 1 - \frac{40.3N(r)}{f^2} dr \tag{3.10}$$

The ionospheric phase delay relative to wave propagation in a vacuum is

$$I_{phase} = t_{travel}^{medium} - t_{travel}^{vacume} = \frac{1}{c} \frac{40.3}{f^2} \int_{raypath} N dr \tag{3.11}$$

TEC is the total number of electrons present along a path between a radio transmitter and receiver that can be expressed by the equation

$$TEC = \int_{raypath} N(r) dr \tag{3.12}$$

Dual-frequency carrier phase and code-delay GPS observations are combined to obtain ionospheric observable related to the (TECs) along the satellite-receiver line of sight (LOS). Pseudorange is applicable to P code. The pseudorange equation in units of length can be expressed as:

$$P_1 = \rho - c\delta(t_r - t^s) + I_1 + T + m_{1m} + b_{1r} + b_{1s} + \epsilon_1 \tag{3.13}$$

$$P_2 = \rho - c\delta(t_r - t^s) + I_2 + T + m_{2m} + b_{2r} + b_{2s} + \epsilon_2 \tag{3.14}$$

By neglecting multipath and thermal noise, the geometric range, clock error and tropospheric delay are canceled.

$$P_2 - P_1 = \Delta p = \Delta I + \Delta b_r + \Delta b_s \tag{3.15}$$

from eq (3.7) p=$\int V_g dt_{path}$ and from eq(3.8) $V_g = c(1 - \frac{40.3N}{f^2})$ and cdt=dr and also from eq(3.12) $TEC = \int_{raypath} N(r)dr$ by substitution and re arranging the variabl.

$$TEC = \frac{1}{40.3}\frac{f_1^2 f_2^2}{f_2^2 - f_1^2}(P_2 - P_1) \tag{3.16}$$

Where p is pseudorange; c is speed of light in vacuum, t^s is transmission time of signal measured by time frame of satellite s , t_r is reception time of signal measured by the clock of receivers r, ρ-carrier phase(m),δt^s and δt_r is satellite and receiver clock error due to the difference in system time; I is ionospheric induced error; T is tropospheric induced error; m_{1m} and m_{2m} is multipath error and ϵ random error. Dual-frequency carrier phase and code-delay GPS observations are combined to obtain ionospheric observables related to the (TECs) along the satellite-receiver line of sight (LOS). To achieve very precise positions from GPS, this ionospheric delay or advance must be taken into account. A GPS operates on two different frequencies f1 and f2, which are derived from the fundamental frequency f_0 = 10.23 MHz: $f_1 = 154.f_0$ = 1575.42 MHz and $f_2 = 120.f_0$ = 1227.60 MHz. The total electron content along the GPS ray path from a satellite to a receiver is known as slant TEC (STEC). TEC is the number of electrons in the slant column with unit squared cross-section in the ionosphere along the signal path that can be expressed in TECU (1TECU = 10^{16} electrons/m^2. The STEC can be obtained from the difference between the pseudo ranges (P1 and P2) of the two GPS signals.

$$STEC_{cod} = \frac{1}{40.3}\frac{f_1^2 f_2^2}{f_2^2 - f_1^2}(P_2 - P_1) \tag{3.17}$$

where f_1 and f_2 are GPS signal frequencies and are equal to 1.57542 GHz and 1.2276 GHz, respectively.

$$\phi_1 = \rho + c(dt - dT) + d\rho + d_T + \lambda_1 N_1 - I_1 + b^s_{\phi_1} + b^R_{\phi_1} + \epsilon(\phi_1) \tag{3.18}$$

$$\phi_2 = \rho + c(dt - dT) + d\rho + d_T + \lambda_2 N_2 - I_2 + b^s_{\phi_2} + b^R_{\phi_2} + \epsilon(\phi_2) \tag{3.19}$$

where

λ, λ_2 Carrier signal wavelength at L_1 and L_2 frequency respectively.

N_1, N_2: Carrier phase integer ambiguities.

$b^R_{\phi_2}, b^R_{\phi_2}$ Carrier phase receiver delays (m).

$b^S_{\phi_2}, b^S_{\phi_2}$, Carrier phase satellite delays.

I_1, I_2 Carrier phase ionospheric delays (m).

$\epsilon(\phi_2, \phi_1)$ Carrier phase measurement noises with multipath errors included (m).

As the pseudorange case, ignoring bias errors, including multipath and thermal noise, the difference between the carrier-phase measurements eliminates the orbital error, geometric range, clock errors and tropospheric delay.

$$\phi_1 - \phi_2 = \lambda N - I + b^S_\phi + b^R_\phi \tag{3.20}$$

where

$$N\lambda = N_1\lambda_1 - N_2\lambda_2, b^S_\phi = b^S_{\phi_1} - b^S_{\phi_2}, b^R_\phi = b^R_{\phi_1} - b^R_{\phi_2}, I = I_1 - I_2$$

The ionospheric phase advance is similar to the ionospheric delay

$$I = \frac{40.3}{f^2} TEC \tag{3.21}$$

$$STEC_{phase} = \frac{1}{K} \frac{f_1^2 f_2^2}{f_2^2 - f_1^2} (L_1\lambda_1 - L_2\lambda_2) \tag{3.22}$$

Where, K=40.3 $m^3 s^{-2}$ is a constant that relates to plasma frequency of electron density λ_1 and λ_2 are the wavelengths corresponding to f_1 and f_2.

3.2 Mapping Function

The ionospheric mapping function is one of the first assumptions to consider when ionospheric corrections are estimated. In many GNSS imaging and navigation systems the assumption is consider a fixed mapping function associated thin single layer surrounding the Earth at a fixed height from the Earth for which all the free electrons in the ionosphere are assumed to be concentrated in a single layer thin shell at the height of the main electron concentration in the ionosphere. In addition to that if we assume there are no lateral or horizontal electron density gradients, the vertical TEC (VTEC) can be simply mapped to the slant TEC. The line-of-sight of TEC values were converted to TECv value by using a simple mapping function and were associated to an ionospheric pierce point (IPP).

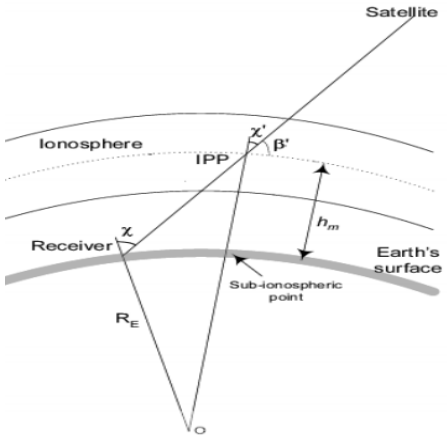

Figure 3.1: Slant to vertical TEC mapping function geometry in the Ionospheric Single Model (SLM).

$$STEC = \frac{1}{\cos\chi} VTEC \tag{3.23}$$

where χ is the satellite zenith angle at the point of intersection of the line of sight with IPP and the multiplier $\frac{1}{cos\chi}$ is called the obliquity factor. The vertical projection of IP on the ground is referred as the sub-ionospheric point (SIP). The satellite zenith angle at the receiver location $\chi\prime$

and at the ionospheric pierce point is related by

$$\sin\chi = \frac{R_E}{R_E + h_m}\sin\chi\prime \tag{3.24}$$

where h_m is height of the ionospheric single layer from the Earth and R_E is the radius of the Earth. This work is done by assuming the ionosphere to be compressed into a thin shell at the peak ionospheric height of 350 km.

$$VTEC = STEC\sqrt{1 - [\frac{R_E \sin\chi\prime}{R_E + h_m}]^2} \tag{3.25}$$

3.3 Data source

The data used in this thesis to study the ionospheric response of CME and CIR driven geomagnetic storm during the selected year is obtained from OMNI data explorer. These data contain IMF (Bz), the solar wind (plasma) speed, flow pressure, flow temperature, Kp-indices, which are accessible using NASAs Space Physics Data center Facility of OMNI Web interface site https://omniweb.gsfc.nasa.gov/form/dx1.html with hourly resolution and Dst-indices from the World Data Center of Geomagnetism, Kyoto http://wdc.kugi.kyoto-u.ac.jp/dst-final/201308/index.html for the selected year from 2013-2017. Based on the data obtained, the graph that shows the CME, and CIR-driven storm have been plotted using mat lab cod by importing the file.

3.4 TEC from dual frequency GPS reciever

TEC derived from GPS signals is a powerful method to studies the ionospheric variability during geomagnetic storms. Total Electron Content data have been obtained from a dual frequency GPS receiver is used to study the ionospheric response during a minor, moderate and severe geomagnetic storm.

Receiver INdependent EXchange (RINEX) formate files with L1 and L2 code and carrier phase

data at 30s epoch rate, downloaded from UNVCO (University NAVSTAR Consortium) http://www.unavco. org/data/gps-gnss/data/ at GPS station that represented with its corresponding four letter code as indicated in Fig.3.2 .

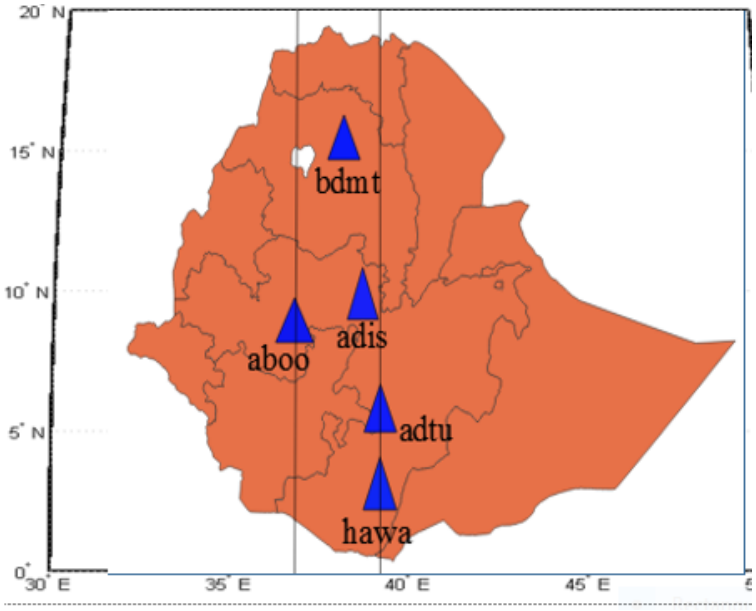

Figure 3.2: Map of the selected GPS station.

The disturbance of TEC is characterized by the percentage of TEC variation over the median quiet day TEC, under the geomagnetic quiet condition (geomagnetic quiet days in the same month were chosen). The quietest day of the month is chosen from world data center for geomagnetismhttp://www-app3.gfz-potsdam.de/kp-index/quietdst/qd201019.html). The GPS-TEC program developed at Boston College was applied to derive the STEC values from each dual frequency GPS receiver of dual frequency signals in L-band at f_1 = 1575.42 MHz, and f_2 = 1227.60 MHz are used to obtained the TEC from each station by using eq (3.17). TECs were transformed into VTEC by assuming the ionosphere to be compressed into a thin shell at a shell height h_m. TECv is obtained from the TECs by use of a mapping function.

$$VTEC = M(e) \times SVTEC \tag{3.26}$$

$$M(e) = \lceil 1 - (\frac{R_E \cos(e)}{R_E + h_m})^2 \rceil \frac{1}{2} \tag{3.27}$$

Table 3.1: Geographic and Geomagnetic Coordimate system.

Station name	Code	Geog.Lat(^{0})	Geog.Log(^{0})	Geoma.Lat(^{0})	Geom.Long(^{0})
Adiss Abeba University	adis	9.035N	38.776E	5.44N	112.56E
Girma House AdmiTullu	adtu	7.86N	38.719E	4.32N	112.33E
Hawassa University	hawa	7.057N	38.499E	4.34N	112.11E
BahirdarUnversity	bdmt	11.6N	37.36E	8.18N	111.57E
Ambo	aboo	8.992N	37.809E	5.55N	111.61E

The ground based dual frequency GNSS receiver constantly logged the two pseudo-ranges (P1 and P2) and carrier-phases (L1 and L2) of the two signals. The raw GPS data from each station logged in observation files is available in RINEX format. The RINEX files were compiled in to 24 hours format by using GPS- Gopi Seemala software. The VTEC values are calculated independently for each station by processing the RINEX observation files in the GPS-TEC analysis software, version Gopi-GR2.9.9 (Seemala). The VTEC file from the program is assembled as Ascii output file in CMN format. The equivalent VTEC values are calculated assuming a thin spherical shell model (Krishna., 2017). To minimize the multipath effects, TEC data corresponding to satellites with elevation angles greater or equal to 20^0 were considered. The vertical TEC were computed by averaging TEC for all satellites in view for a specific station by using hourly running average to get a single curve for the entire day. To study storm time modifications of VTEC. The ionospheric responses were then identified by calculating the deviation of VTEC (ΔVTEC) values using the equation.

$$\Delta VTEC = \frac{VTEC - VTEC_{median}}{VTEC_{median}} \times 100\% \tag{3.28}$$

Where VTEC is the total electron content value for all satellite that are observed in 30-second resolution interval averaged in to 24 hours for all satellite and the outlier removed by using eq (3.2)

$$|VTEC - VTEC_{mean}| > 2 \times \sigma VTEC \tag{3.29}$$

$VTEC_{mean}$ is the monthly median of ten international quiet days in the month,where the storm occurs and ΔTEC-is the deviation of VTEC. In this work I have followed the same method used in previous studies (Matamba et al., 2015).

During the analysis period from January 2013 to December 2017, we observed 31 moderate and 11 intense storms in the Solar Cycle 24.

Table 3.2: Number of Storms that occurred in the year 2013-2017.

Year	2013	2014	2015	2016	2017
Intense storm	2	1	4	2	2
Moderate storm	6	7	8	7	3
Total	8	8	12	9	5

Chapter 4

Result and Discussion

Geomagnetic storm is a major disturbance of Earths magnetosphere, due to the interaction of south ward interplanetary magnetic field with the earth magnetic field. The interaction leads to induce aditional energy to the magnetotail of the magnetospher. These energy leads to vary (desturb) the earth magnetic field in some extent. The variation of the earth magnetic field is considered to be geomagnetic storm.

Out of 42 total geomagnetic storm occured during the analysis period, We have only select the intense storm and more moderate storms with $-100 < Dst_{min} < -88nT$ that have an avaliable GPS TEC data over the selected GPS station. Since weak and less moderate geomagnetic storms have no significant effect on ionosphere and magnetosphere, they are not discussed in detail. A detailed study has been carried out for the moderate storm with $Dst < -88$ nT and intense storm that have an available GPS TEC data. During the analysis period we have three moderate storm and seven intense storm have been available TEC data over the selected GPS station as indicated in Table 4.1

We use the same method Matamba and Habarulema. (2018) in order to quantify the response of TEC during CME and CIR-driven geomagnetic storms. The quiet time ionospheric variability of TEC data were determined as $\pm 45\%$. A geomagnetic storm is produce an ionospheric storm if ΔTEC exceeds $\pm 45\%$ for at least 3 hr. TEC variability that fell with in $\pm 45\%$ on any given storm period was considered as not significant (NS) or quiet. If the deviation exceeds $\pm 45\%$ is positive and negative ionosphere response and also if the deviation exceeds 45% followed by depressed -45% is positive-negative and negative -positive.

Table 4.1: Phase of minimum Dst index occurance.

Year	Month	Day	Dst(nT)	Time(UT)
2013	March	17	-132	20:00
	Jun	1	-124	08:00
2014	February	20	-119	08:00
2015	March	17	-223	23:00
	January	7	-99	11:00
	Jun	23	-204	04:00
2016	January	1	-110	01:00
	Jun	19	-93	17:00
	March	7	-98	21:00
2017	May	28	-125	07:00

4.1 Yearly distribution of CME and CIR

The performance of CMEs and interplanetary magnetic field (IMF) conditions cause the development of geomagnetic storms during solar maximum (Matamba et al., 2015). However, during the declining phase, moderate geomagnetic storms under different IMF conditions are generated by the high-speed solar wind stream from the coronal hole.

Fig. 4.1 indicates the number of CME (green bar) bar, CIR (blue bar), total geomagnetic storm (red bar) over the selected year (2013-2017), and the number of sun spot during the solar cycle 24 (2008-2018) indicated on the bottom panel. As shown from the Fig.4.1 bottom panel the sunspot number decline from 2013 up to 2018. The number of CIR maximum during the decline phase of the solar cycle 24, where as the the number of CME is minimum (Wyllie., 2007). The number of CME driven storm is greater in 2015 as compaired the rest one.

4.2 Seasonal distribution of CME and CIR

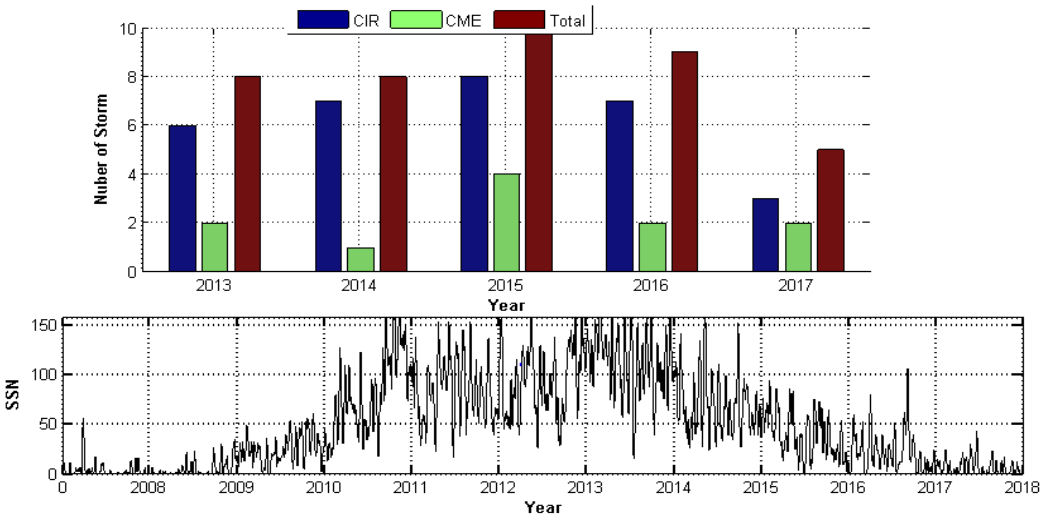

Figure 4.1: CIR (blue bar), CME (green bar), and total geomagnetic storm (red bar) with yearly Sunspot number (black) bottom panel plot .

Fig. 4.2 shows the number of CIR (blue bars), CME-driven (green bars) and total geomagnetic storms (red bars) per month with the corrosponding daily sunspot number indicated on the bottom panel. A high number of CIR driven storm occured during the decline phase of solar cycle (solar minima) and CME is during solar maxima (Adeniyi et al., 1986). The number of CME driven storm is greater during march equinox and June solistic season as compaired the rest one.

4.3 CME and CIR-driven geomagnetic storm events

The difference between CME and CIR-driven storms hade been summarized (Borovsky and Denton., 2006). Based on Dst index, geomagnetic storm can be grouped in to weak ($-50nT < Dst < -30nT$) to moderate ($-100nT < Dst < -50nT$) mostly driven by CIR and intense ($Dst < -100nT$) driven by CME due to the presence of large southward-directed Bz (Wyllie., 2007; Liu et al., 2015; Huttunen and Schwenn., 2002). CIR- and CME-driven storms can be classified based on the features of proton temperature, solar wind speed, magnetic field, proton density, and recovery phase (Dugassa et al., 2020b). CME-driven storms can be identified by the stronger magnetic field, the enhanced solar wind speed, low proton temperature, and high

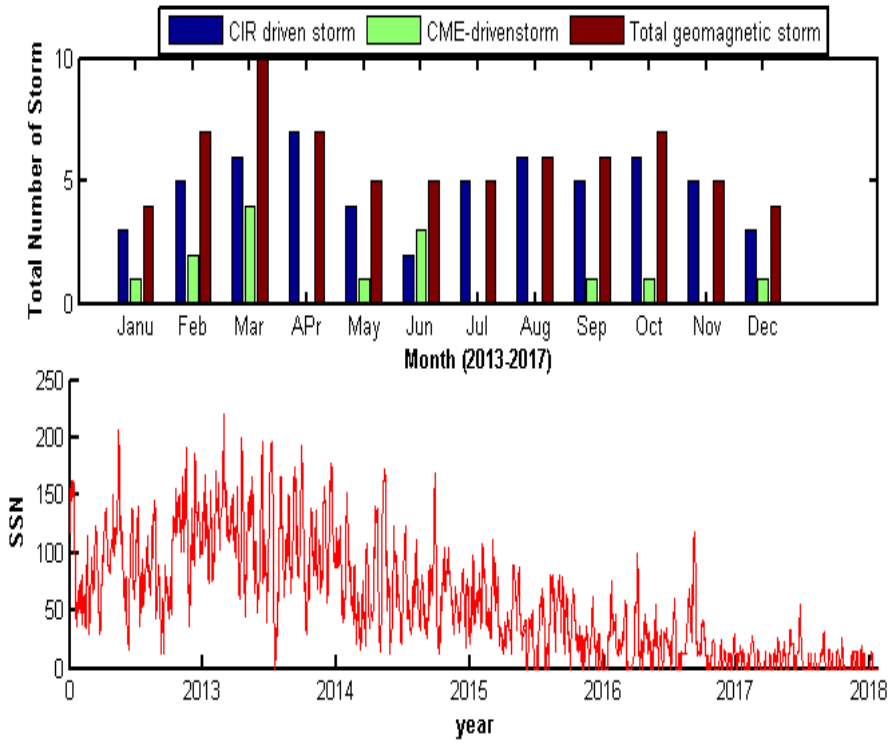

Figure 4.2: CIR (blue bar), CME (green bar), and total geomagnetic storm (red bar) with yearly Sunspot number (red plot) bottom panel .

ratio between the densities of alpha particles, and short recovery phase that lasts one or two days. Fig. 4.3 shows an example of an intense geomagnetic storm driven by CME during 15-19 March 2015. It illustrates Dst index (nT), Kp index, proton temperature (K), solar wind speed (km/s), IMF-Bz component (nT), magnetic field $|B|$ (nT), proton density (ρ, cm^{-3}), and flow pressure (nPa). An intense geomagnetic storm occurred on 17 March 2015 at a time of 04:45UT(07:45LT) and reached a minimum Dst index of-223nT at around 23:00 UT($\sim$ 2:00 LT) with Kp index of 7.7. The temperature increased from $\sim$ 4.529$\times 10^4$ K to $\sim$ 8.073×10^5 K after sudden storm commencement. The solar wind speed increased from $\sim$ 413 km/s to $\sim$ 614 km/s. The Bz component turned southward, from 20.1 nT (05:00 UT) (08:LT) to $\sim$ -16.3 nT (08:00 UT) (11:00 LT) during geomagnetic storm. $|B|$ decreased from 21.9 ($\sim$ 05:00 UT) to $\sim$ 19.6nT ($\sim$ 07:00 UT), density increased from $\sim$ 15.42 $^{-3}$ to (05:00) to 33.7 cm^{-3} (03:00) and short recovery phase

that lasts two days to return to normal quiet position. On the other hand, the main features of

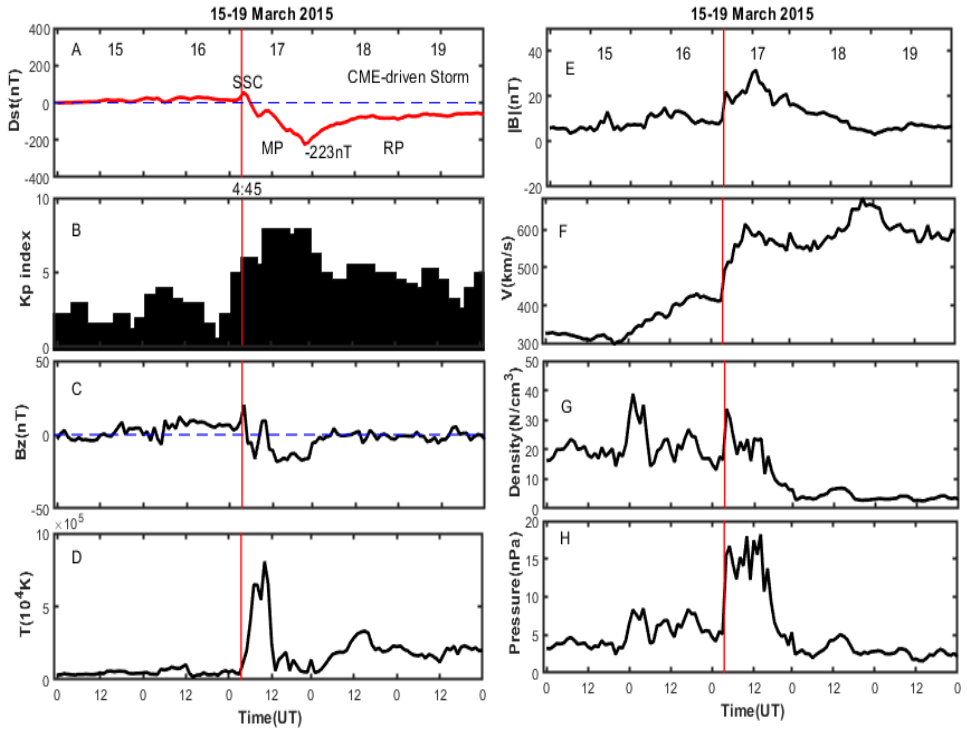

Figure 4.3: Variation of Dst and Kp indices, temperature, solar wind speed, magnetic field $|B|$, Bz magnetic field component, density, and flow pressure for 15 to 19 March 2015. The vertical red line on the figures indicates the sudden storm commencement for coronal mass ejection-driven storm.

CIR-driven storms are an enhancement of proton temperature, an increase of solar wind speed, a compression of the magnetic field, Bz component fluctuates throughout interval due to high speed and proton density increased as well longer duration recovery phase as it compared with CME phase (Matamba and Habarulema., 2018).

Fig. 4.4 illustrates an example of CIR-driven storm for the period of 18-22 January 2016. The Sudden Storm Commencement (SSC) occurred at 21:57 UT (00:57LT) (LT=UT+3) on 18^th,2016. Immediately after SSC the flow of solar wind speed increased to 366km/s from 333km/s, IMF(Bz) component depressed from -1.3 to -6.5nT and fluctuatly increased until it reaches the initial phase

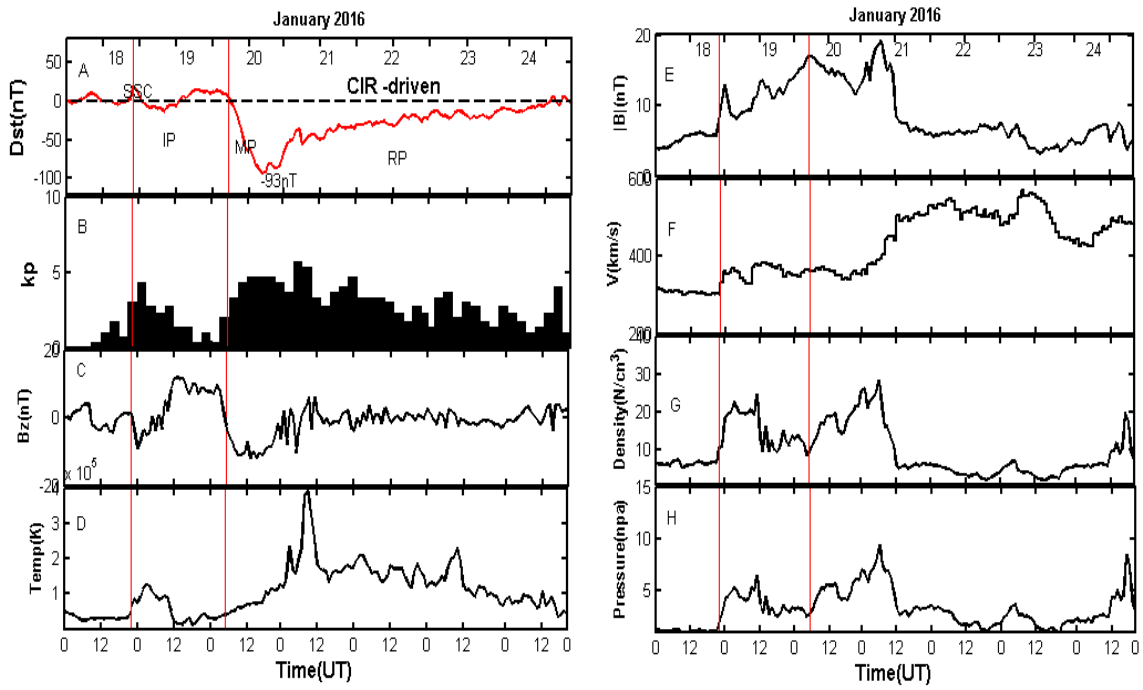

Figure 4.4: Variation of Dst and Kp indices, temperature, solar wind speed, magnetic field $|B|$, Bz magnetic field component, density, and flow pressure for 18 to 22 January 2016. The vertical red line on the figures indicates the sudden storm commencement at21:57UT, and the begining of the main phase of CIR driven storm. Ip, Mp, and RP is intial, main and recovery phase ,CIR-Corotating interactio region

. After the intial phase Bz turns south ward. A moderate geomagnetic storm occurred on 20 January 2016 with a minimum Dst index -93nT (16:00 UT)(19:00LT) with 4.7 Kp value. The region between the two vertical lines (red) in Fig. 4.4 indicates the initial phase of a geomagnetic storm. Immediately after the initial phase, an increase in proton temperature 1.424×10^4K at around ($\sim$13:00 UT) on the mid-day to 3.906 $\times10^5$(K) on the afternoon at around 08:00UT after one and half days, Solar wind speed ($\sim$362 to $\sim$547) km/s, proton density ($\sim$9.4 to $\sim$ 18.9 cm^{-3}), and flow pressure ($\approx$ 2.67 to $\sim$ 5.61 nPa), magnetic field $|B|$ compressed from ($\sim$ 16.9 to $\sim$11.5nT), Bz turns south ward from 0.6nT ($\sim$04:00 UT) to -11.4nT ($\sim$ 09:00 UT) and the storm

took a longer three and half days to return to its quiet position. From the above two Figure, CIR driven storm tooks more time to return to its quiet position as compaired with CME (see Fig.4.3, 4.4).

4.4 CIR Driven Event

4.4.1 Geomagnetic activity of 5-9 January 2015

Fig. 4.5 shows Dst, and Bz indices top panel, kp-upper-middle panel, and ionospheric deviation lower middle and bottom panel of each plot. The blue vertical line is the onset time of the storm, CIR-Corotating interaction region. On january 4, 2015 less moderate storm occured at around 17:00UT with minimum Dst(-62nT). As shown from Fig. 4.5 on top panel, day 5 and 6 are the recovery phase of january 4,2015. On 7 January 2015, CIR driven event expected to on set and hit the earth's magnetic field at $\sim$ 06:16(UT) (09:16LT). During this time the Bz turns south ward with a minimum value -17.4nT. Following the south ward turnning of Bz, geomagnatic field activity of the earth is highly depressed to a minimum -99nT at 11:00UT with the corrosponding kp value 6.

From Fig. 4.5 positive -negative ionospheric response observed before SSC at each station. Becouse day 5 and 6 were the recovery phase of january 4,2015. A significant positive response observed during the recovery phase. The maximum deviation of VTEC at each station were (bdmt, 107.6%), (aboo,165.6%), (hawa, 125%), (adtu, 111%,), and (adis,136%). This indicates the total electron content was highly suppress during march 7,2015.

4.4.2 Geomagnetic activity of 18-22 January 2016

Coronal holes are a region in the sun's atmosphere where the magnetic field opens up and allows solar wind to escape out in to the interplanetary space with a high speed. On 18 january 2016 the IMF-Bz turns north to south at around 10:00UT and very quiet storm observed and turns north ward. After a few hour the onset of the storm started on the same day at 21:57 UT. At this time

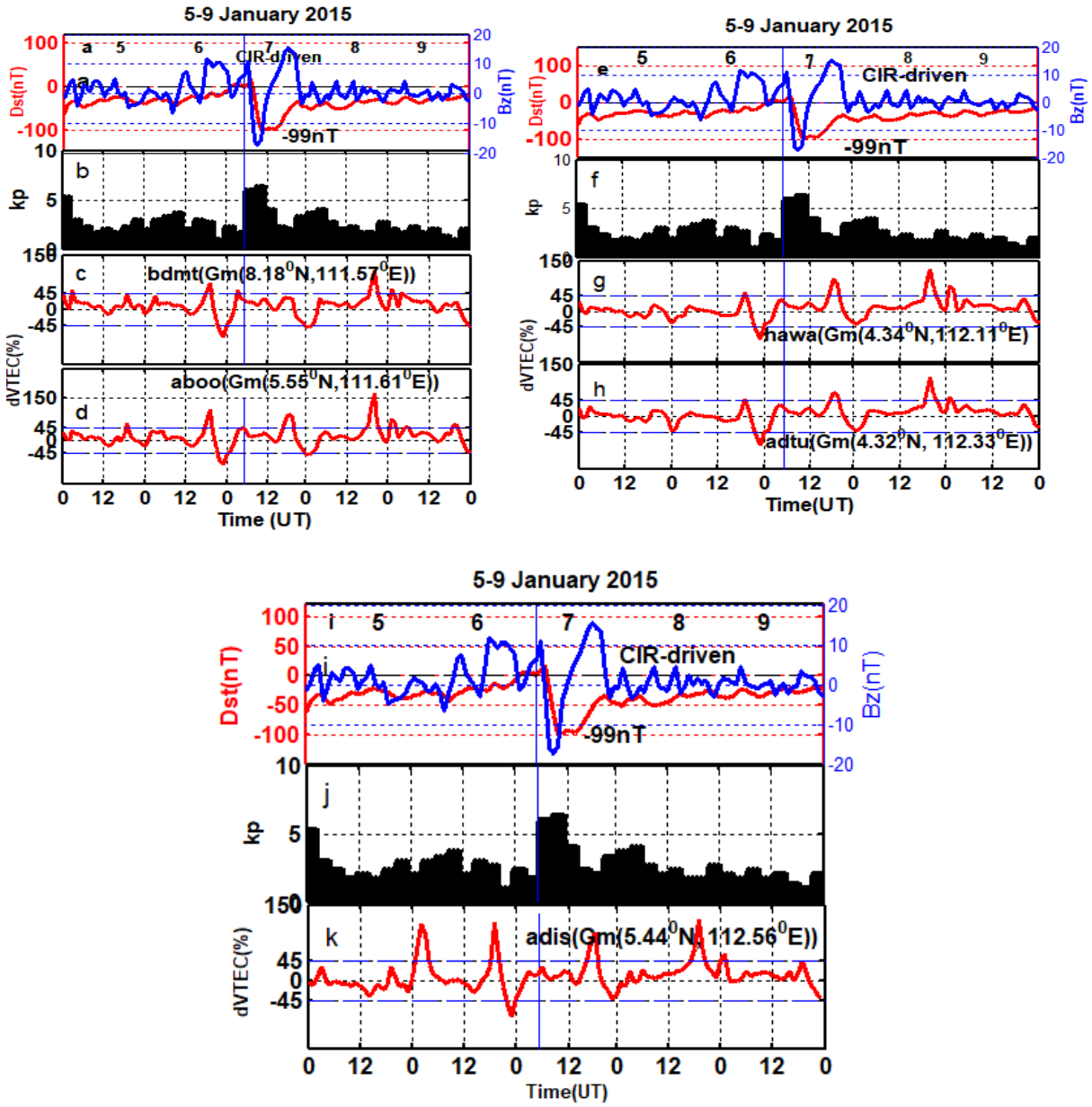

Figure 4.5: Dst and Bz top panel, kp- upper middle panel, Ionospheric deviation lower-middle and bottom panel of 5-9 January 2015. The blue vertical line is the onset time of the storm, Mp and Rp is main and recovery phase of the storm, CIR-Corotating interaction region.

Bz turns south ward and attains a minimum value -9.2 nT (01:00UT) and turns north -south ward flactuation for 9 hour and remain north ward for 19 hour.

During the main phase Bz turns south ward and attain a minimum value -11.8nT at around 16:00UT with the corrosponding minimum Dst index (-93nT), and 4.7 Kp value at the end of the main phase as shown in the Fig.4.6 top panel. This storm is chatagorised under moderate storm that driven by CIR. As shown from Fig.4.6 before the onset of the SSC a positive ionospheric response obserbed at **aboo**, and **adtu** . Bz fluctuatly vary in north-south direction and attain minimum value -10.3nT with the corrosponding 5.7 kp value at 05:00 UT on day 21.

On the main phase $\Delta VTEC$ was enhanced at **bdmt** (74.7%), **aboo** (95.91%), **adtu** (134.9%), and **adis** from (20:00 - 24:00)UT respectively. Dst depressed as IMF-Bz turns south ward as shown in Fig.4.6 top panel. On the other hand it also enhanced to 90.87% at **bdmt**, 135.4% **aboo**, 151.6% **hawa**, 115.1% **adtu** and 100.1% at **adis** respectively . These enhancment of ionospheric activity takes place before sun rise accelerated due to DDEF.

4.4.3 Geomagnetic activity of 5-9 March 2016

To describe the effect of Geomagnetic storm event on March 7^{th} 2016, Dst and Bz top panel, kp value middle panel, and ionospheric deviation lower-middle, and bottom panel for five consecutive days from 5-9 march 2016. The onset of the storm observed on 6 march 2016 with SSC at $\sim$ 21:57UT when Dst startes sharp spike above the quiet condition as shown in the Fig.4.7 top panel. On 7 march 2016 Bz starts to decline in to south ward and reached a minimum value -12.7nT at around 21:00UT. Following the south ward turning of Bz, energetic particle and momuntum deposited in to magnetosphere and affects the earth magnetic field to depleted a minimum value -98nT at 21:00 UT on the same day with corrosponding kp value 6.3. These event is considered as a moderate storm that driven by corotating interaction region.

As shwn from Fig.4.7, during the main phase positive ionospheric deviation was observed at **hawa**, and non-significant at **bdmt**, **aboo**, and **adis** respectively. After the main phase small enhancement of ionpspheric index activity observed at **bdmt**, and **aboo**, non-significant at **adis** and positive- negative response at **hawa**. During the geomagnetic storm the depression and enhans-

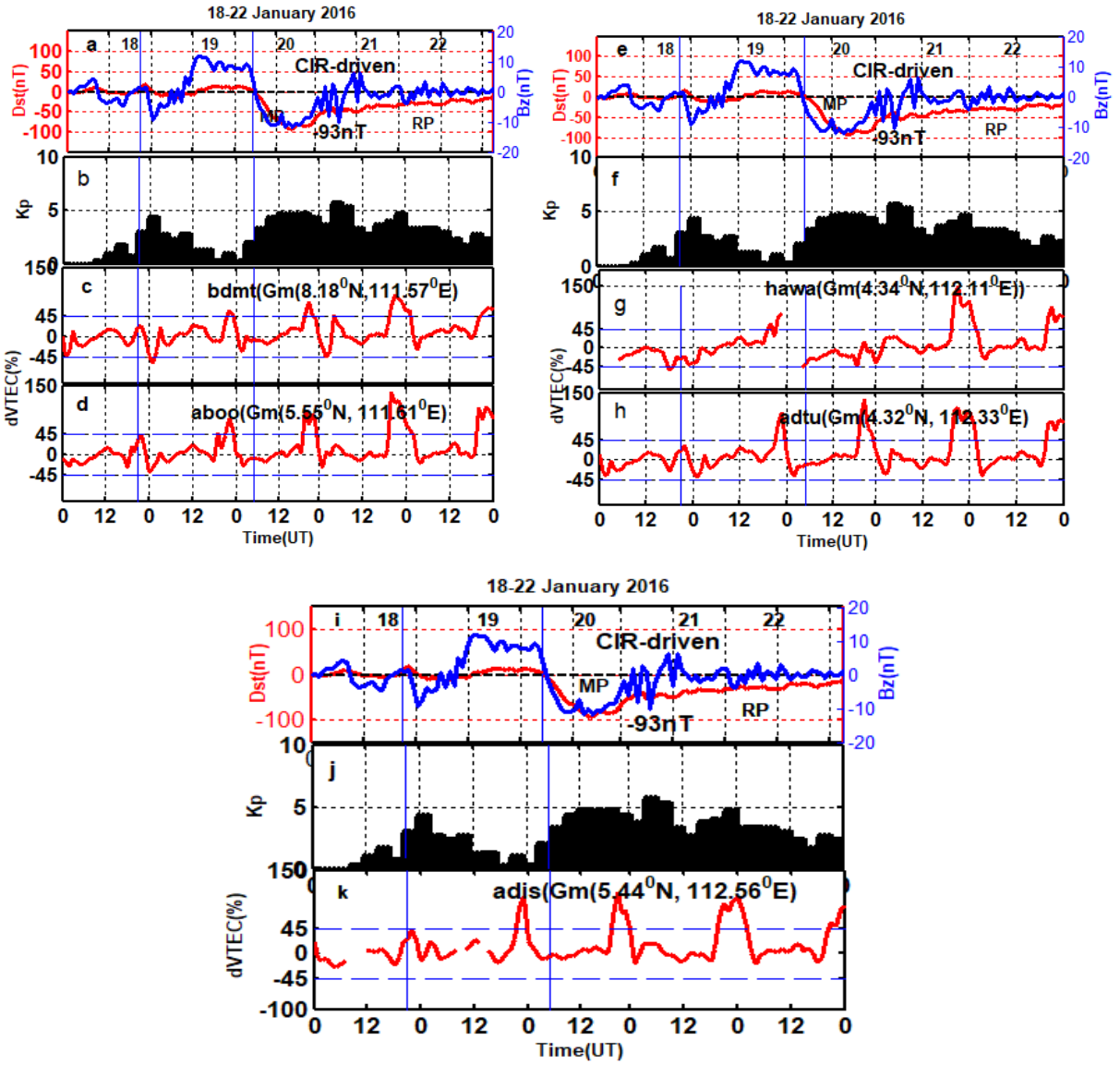

Figure 4.6: Dst and Bz top, kp upper-middle and ionospheric index activity lower middle and bottom (left -right) panel plot 18-22 January 2016. the two vertical solid line plot is the SSC, and intial the phase of january 20. Mp, and Rp is main and recovery phase. SSC-sudden storm commencement.

ment of VTEC affects the navigational, and communicational system (Chakrabort et al., 2015). The ionospheric variability affected by PPEF, and DDEF, neutral composition change and oxy-

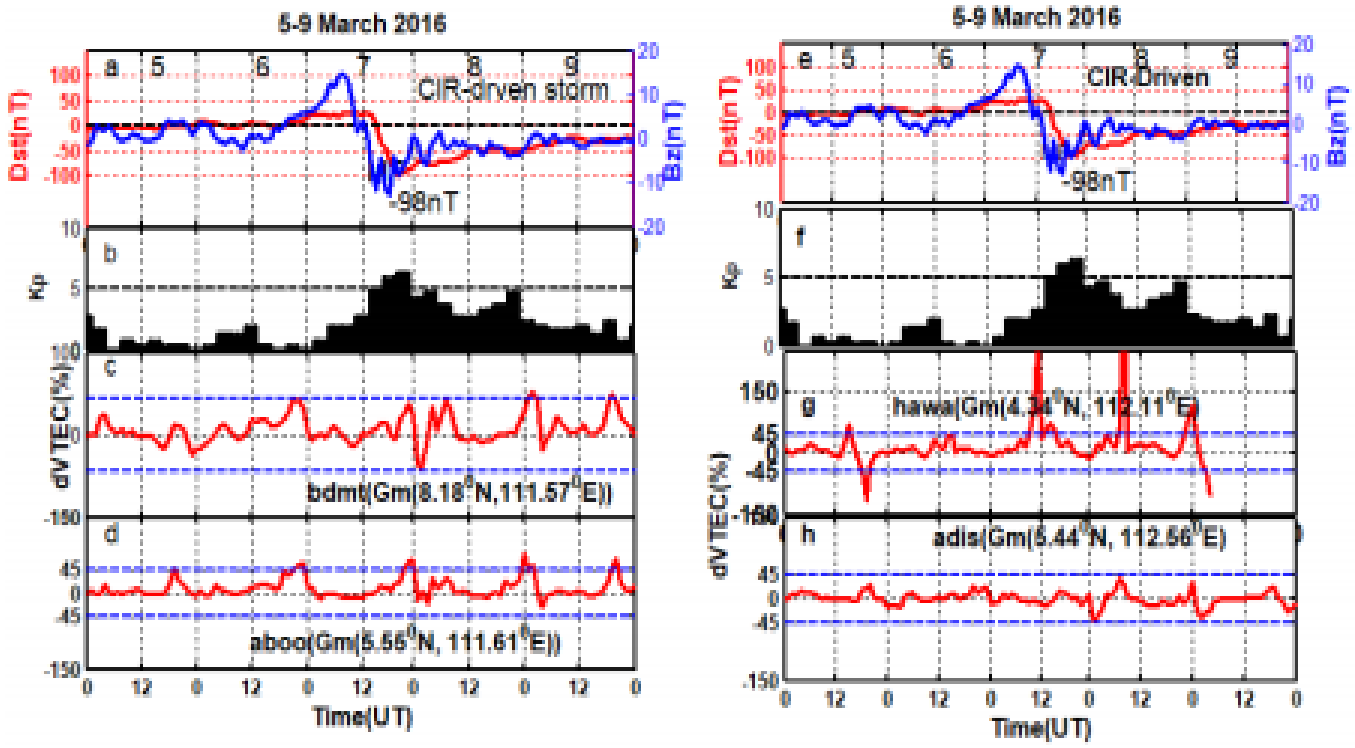

Figure 4.7: Dst and Bz top panel, kp upper-middle panel, ionospheric index activity lower middle, and bottom panel of each plot of 5-7 march 2016. Horizontal blue line on the lower middle and bottom panel is the boundary limit of non-significant ionospheric response, CIR-corotating interaction region.

gen nitrogen ratio. During the day time PPEF is flow due to east, and responsible for positive ionospheric response, while DDFE is west ward during the day time (Dugassa et al., 2020b). During the night time DDEF is east ward that lead to affect the ionospheric dynamics of the upper atmosphere. DDEF are more active during the storm recovery phase. The positive response obserbed at bdmt, and aboo atributed due to DDEF becouse of the response has been occured during the night time.

4.5 CME-Driven Storm

4.5.1 Geomagnetic activity of 15-19 March 2013

This section presents the characteristics of the geomagnetic storm occurred during the period of 15 -19 March 2013 with the corresponding Dst index, IMF-Bz(Geocentering solar Magnetic feild), Kp value. CME was erupted from the solar active region on 15^{th} March 2013 with SSC at 5:26 UT (8:26LT) following the southward turning of IMF Bz. It attains a minimum value -5.6nT at 06:00UT and recover immidiatelty. On March 17 an intense CME with M-class solar flare emmision erupted from the active region of sun spot AR1696 with with a speed 625.8km/s and creates SSC (shock wave) at 06:00UT. During this time energetic particles and interplanetary magnetic field enter to the earth magnetosphere and desturbs the earth magnetic field by creating an extra field on to the magnetotail. As shown in the Fig. 4.8 Dst index (red), and IMF-Bz (blue) top panel, kp -upper middle panel, ionospheric index activity upper-middle (**bdmt**), lower-middle panel (**aboo**), and bottom panel (**adis**) respectively.

Bz turns southward significantly after SSC and attains a minimum value -14.4nT at (09:00UT) . At this time geomagnetic field disturbance obserbed with a minimum Dst-index-66nT (09:00UT). After a hour Bz turns to north-south perturbation until it reach -0.8nT (14:00UT) and also back to south-ward direction and reached a minimum Bz value -11.6nT at (18:00UT) and turns north ward at (00:00UT). The rapid fluctuation of Bz further decreases the geomagnetic field with a minimum value -132nT (20:00UT) at the end of the main phase with the corresponding 6.7 kp-value. These event is considered as intense storm with its Dst <-100 nT and Kp $>$ 6. Fig.4.8 shows a positive ionospheric respose observed at each station at around the end of the main phase before sun rise. During the recovery phase positive response observed at **bdmt** and non significant at **aboo**, and **adis** respectively. Before sun rise the maximim ionospheric deviation observed (107.3%, **bdmt**), (81.12%, **aboo**), and (76.43%, **adis**) during the main phase, and (62.43%, **bdmt**) on the recovery phase. The ionospheric storm effects in the equatorial latitude are due to the modification of equatorial ionization anomaly (EIA) by electric fields and winds, neutral composition changes, and wind-induced transport. The daytime positive ionospheric storm ef-

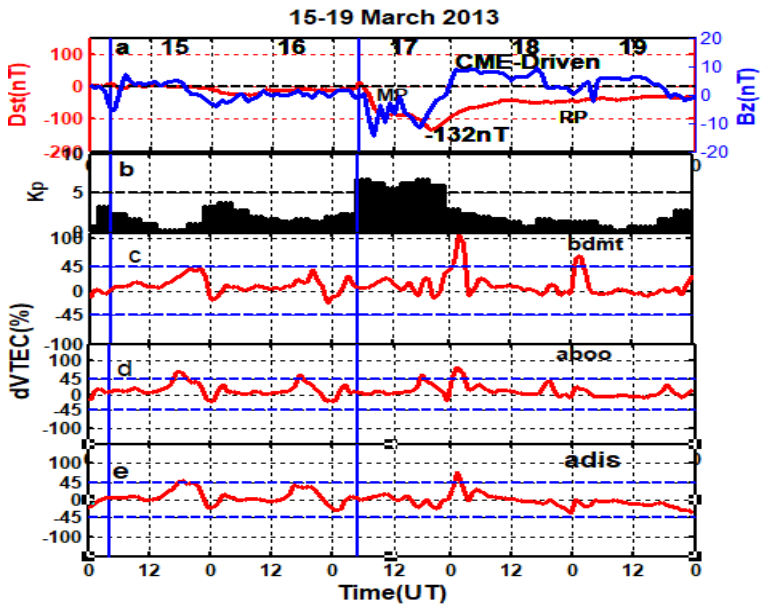

Figure 4.8: Dst, and Bz top panel, kp upper middle and ionospheric deviation lower middle, and bottom panel of 15-19 March 2013. The blue vertical line is the SSC. Mp and Rp are main and recovery phase of the storm , CME -coronal mass ejection. horizontal blue line over the lower plot is upper and lower limit of non significant ionospheric response.

fects over the low (equatorial) latitude, and middle-latitude ionosphere have been atributed due to prompt penetration electric field (PPEF) (Adeniyi et al., 1986; Matamba and Habarulema., 2018). Neutral winds, penetration of electric fields, and neutral composition are responsible for the positive ionospheric storm effects in the low latitudes.

4.5.2 Geomagnetic activity of 30 May-3 June 2013

This section shows the characteristics of the geomagnetic storm occurred during the period of 30 May-3 June 2013 with the corresponding Dst, and IMF Bz top panel, kp upper- middle panel and ionospheric variability on lower- middle and bottom panel of each plot .

On Fig. 4.9 a small spike of Dst index was observed at around 16:18 UT (19:18LT) on May 31, 2013. After a certain hour the spike turns south ward following the direction of Bz component.

The main phase starts on (1) June 2013 at arouna 02:00UT with a minimum Dst value -124nT and kp=7, that lasts 07:00h on the same polarity, and flactuatly vary with north-south perturbation in a small aplitude. After the end of the main phase on 10:00 UT of the same day Dst index returns in to its quiet condition. As shown in the top Fig.4.9

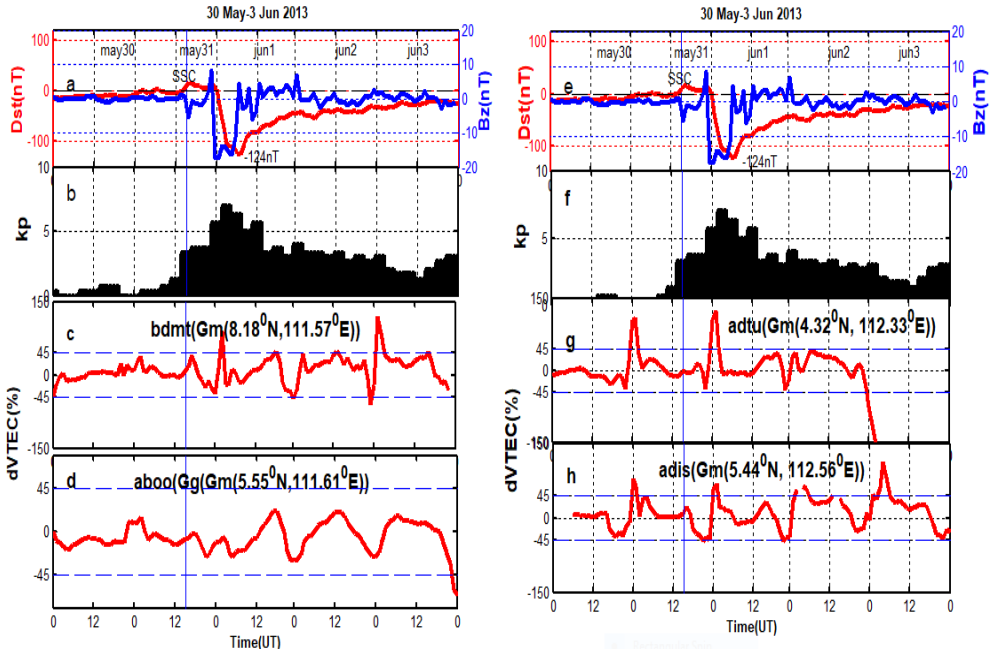

Figure 4.9: Dst and Bz top panel, Kp middle panel, ionospheric deviation VTEC at **bdmt** , **aboo**, **adtu** and **adis** lower plot . Vertical solid line is sudden storm commencement. Mp and RP are main and recovery phase of June 1, 2013.

the main phase last $\sim$ 04:00h, while the recovery phase tooks two and half day's to returt to its quiet condition. This event is considered as an intense geomagnetic storm with Dst <-100nT, and kp $>$ 6 (Huttunen and Schwenn., 2002). The maximum ionospheric vTEC variability at bdmt, aboo, adtu, and adis (c, d, g,h). During the main phase a significant positive ionospheric response observed at **bdmt** (89.08%), **adtu**(122.8%), **adis** (68.98%), and non-significant at **aboo**. Negative -positive at **bdmt**, negative at **adtu**, slight positive at **adis**, and non significant response at **aboo** were obserbed during the recovery phase of june 1,2013. The response of hawa GPS station may not menshed due to TEC data inavaliability during june (1). The maximum

ionospheric variability observed during the recovery phase at **bdmt** is due to that of ionospheric index activity vary with time and sation.

4.5.3 Geomagnetic activity of 17-21 February 2014

Fig. 4.10 shows the quiet day running median with the observed VTEC value. As indicates on the legend the red plot is the observed VTEC value, while the blue one ie monthly running median of quiet day. The two plots moves equivalently during the morning, and far far apart after the mid day. These indicates the ionospheric irregularity is greater after the midday untill the evenning. As shown the over all plot the maximum ionospheric irregularity observed on 19 february 2014 as compaired the day befor and after 19.

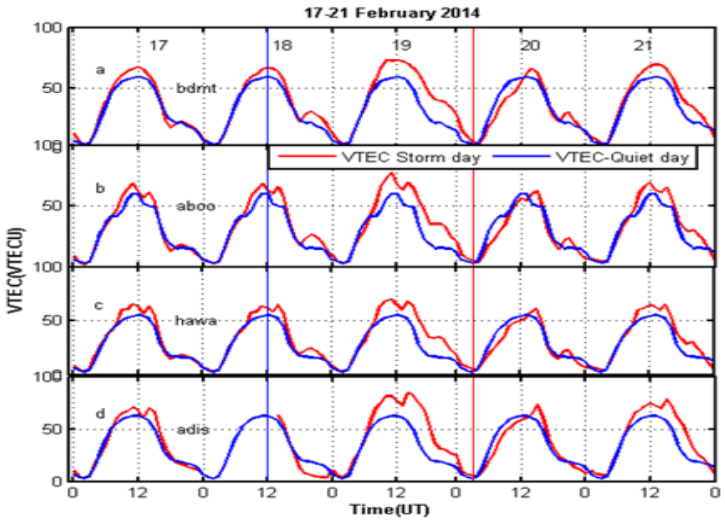

Figure 4.10: Diurnal variation of VTEC monthly quiet day running median with the baground

Fig.4.11 Dst and Bz top panel, kp upper middle panel, ionospheric deviationy (Δ VTEC) lower-middle panel, and bottom (left -right) panel over the selected Gps station of 15-19 february 2014. Befor the onset of the intial phase Bz is in the south -north orientation. After the intial phase Bz highly turns in to south ward and reached a minimum value -12.9 nT at 05:00 UT, and turns north -south flactuation until the begining of the recovery phase. Following the south ward turning of Bz, the geomagnetic field was deperessed to a minimum value -119nT on february

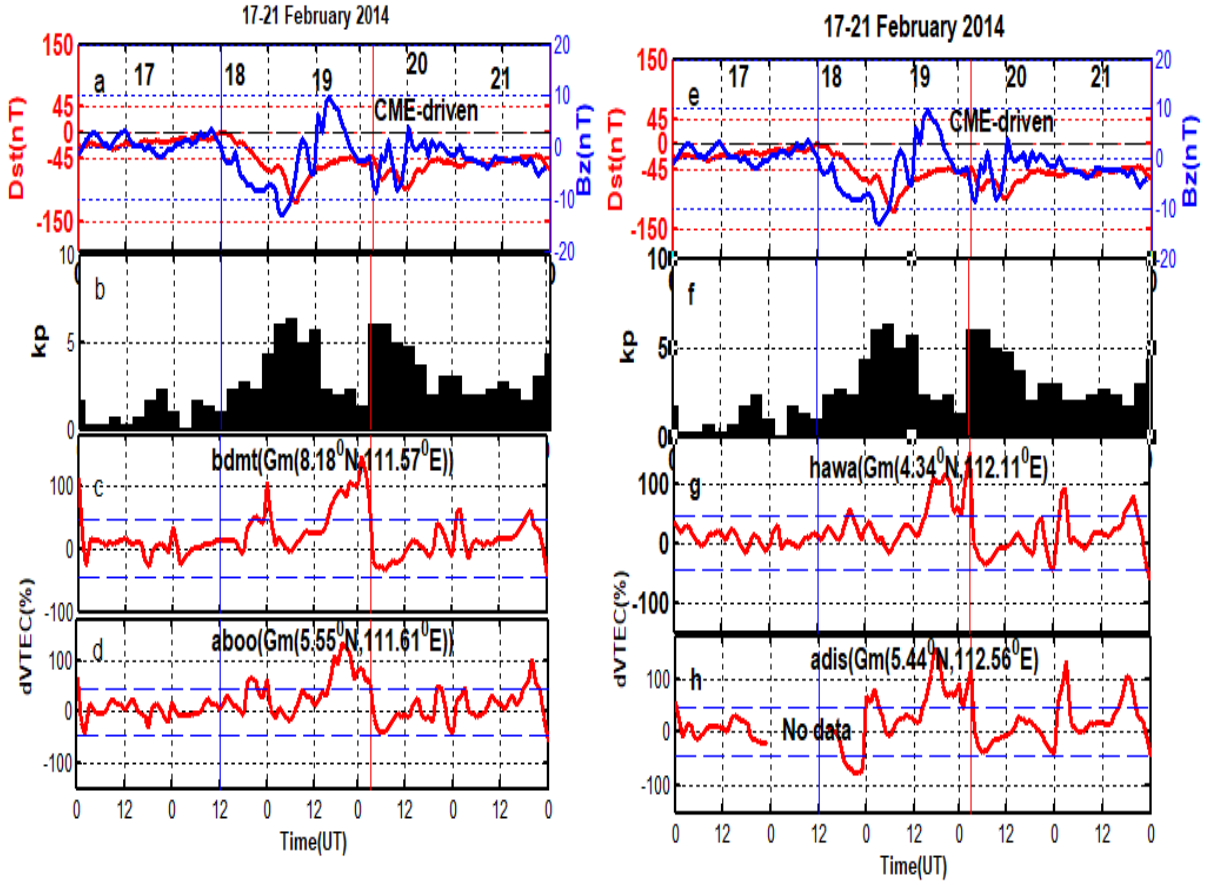

Figure 4.11: Dst and Bz top panel, kp-middle panel, ionospheric index activity (deviation of VTEC) lower middle and bottom panel of 17-21 february 2014 . The blue and red vertical solid line is the intial phase, and sudden storm commencement. The two horizontal blue line is the the upper and lower limit of non -significant ionospheric response, CME -coronal mass-ejection.

19 at around 08:00 UT. On february 20, Bz again turns south ward, the second sudden storm commensment observed and turns south-north flactuation.

During the main phase from 17:00-05:00 UT small enhansment of ionospheric activity obserbed at **bdmt**, **aboo**, **hawa**, and negative- positive at **adis**. A significan enhancment of ionospheric deviation obserbed during the recovery phase on each station as shown in the Fig.4.11. The maximum ionospheric deviation obserbed during the recovery phase from 18:00UT-03:00UT. The deviation 190% at **hawa**, 110% **adis**, 116% **aboo**, and 141% **bdmt**. DDEF are more active during the recovery phase . The night time positive ionospheric storm observed at each station during the recovery phase of the storm could be attributed due to the DDEF effect. Out of thus the maximum percentage deviation observed at hawa. The effect of geomagnetic storm related with geographic lattitude. The area nearly close to the equator is more affected by geomagnetic storm than others. out of the station we use hawa more highly near to the equatore than others. Due to this its ionospheric variability is greater as compaired the rest one.

4.5.4 Geomagnetic activity of 15-19 March 2015

Fig.4.12 shows the variation of Dst, and Bz indice top panel, kp upper-middle panel, and ionospheric deviation lower-middle, and bottom panel of each plot during 15-19 march 2015. The vertical solid line indicates the SSC. The two blue horzontal dash plot is the upper and lower limit of queit condition. On 17^{th} March, 2015, an incoming CME ejected from the active region of sunspot AR2297 in to space with a speed of 599.3 km/s, and hits the Earth's Magnetic field at around 04:45 UT. From Fig. 4.12 IMF-Bz was disturbed and forced to point up northwards from 3 nT to 20.1nT, and turned south-north fluctuation untill it reached a minimum value -16.3nT(08:00UT), and -18.1nT(14:UT) on the same day. As Bz turns south ward energetic particle enter to the earth magnetosphere and desturb the earth magnetic field to depressed a minimum value -223nT on the main phase at aruond $\sim$ 23:00UT with (kp=7.7). These the minimum Dst$<$-100nT with kp value $>$ 6 is chatagorised to the intense storm(sever) caused by CME driven. As shown from the Fig. 4.12 the ionospheric deviation hihgly suppressed during march 17, 2015 at

each station over the main phase of the storm. The response greater at **hawa**, **adtu**, **aboo** and **bdmt** and **adis** respectively.

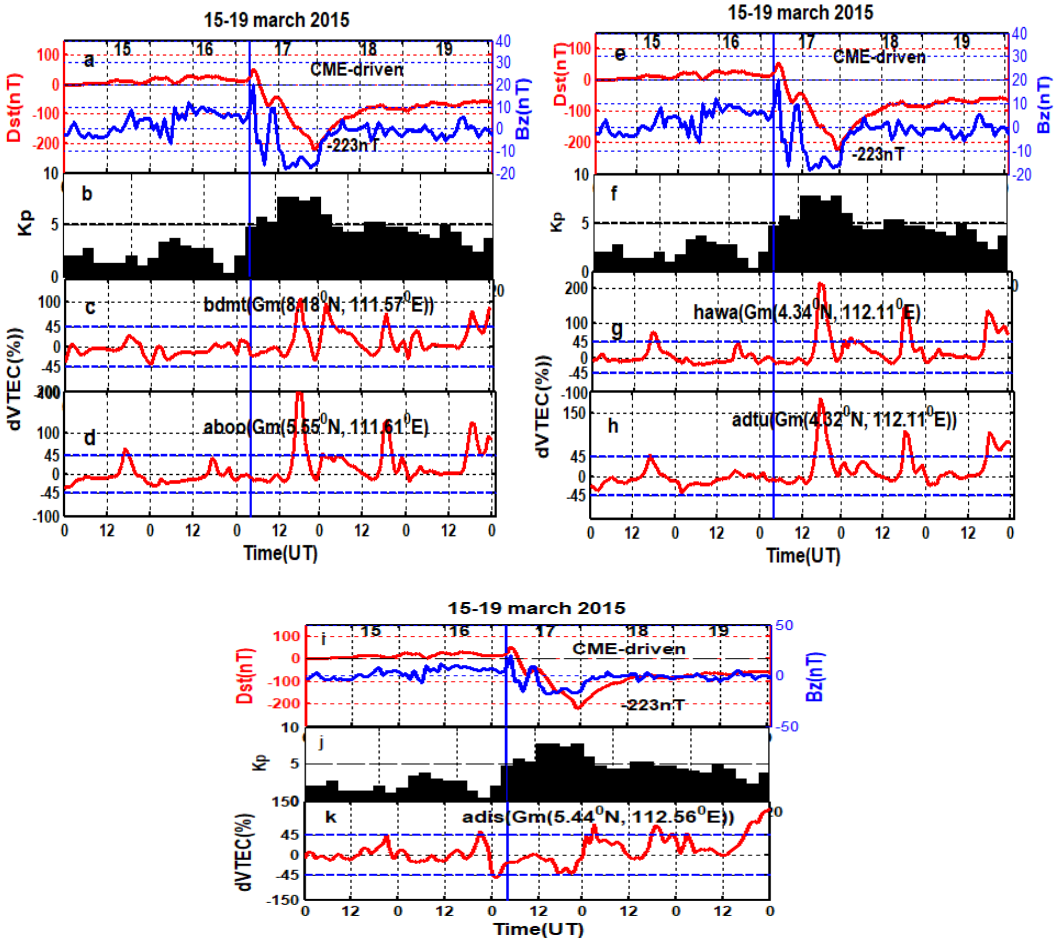

Figure 4.12: Dst and Bz top, kp upper- middle, and ionospheric indice activity lower-middle and bottom panel of 15-19 March 2015 .The solid blue vertical line is the onset time of the storm, CME-Coronal mass ejection.

The recovery phase started after the end of the main phase up to the end of 19^{th} of the same month. During the recovery phase the ionospheric respose is positive for each station (see Fig.4.12). As shown on each Fig the ionospheric response is greater at hawa, adtu and aboo respectively.

4.5.5 Geomagnetic activity of 21-25 June 2015

The variation of Dst, and Bz top panel, kp upper middle panel, and ionospheric deviation lower middle and bottom panel of each Gps station. A strong CME driven storm ejected out from the sun, and hits the earth magnetic field on 21 jun 2015 with SSC at 16:44 UT folowing south ward turnning Bz component . The intial phase starts after the first SSC. The ionospheric response slightly enhanced at aboo, and depressed at hawa, but non-significant at bdmt, adis, and adtu. After small perturbation Bz highly depleted in to south ward, and reached a minimum value -26.3nT with a maximum rising kp (8.3) value. At the end of the intial phase, the second SSC observed on 22 jun 2013 at 18:00 UT. The Bz value then again depleted to the minimum value -21.3nT with the corosponding -204 nT Dst index, and kp value(7.7).

As shown from the 4.13 the ionospheric index activity vary highly at aboo, and slightly depleted at bdmt, hawa, adis, and adtu. Negative ionospheric response observed during the main phase on both station except aboo. Both positive- negative response observed at aboo with a maximm depression (-93.3%) at 11:00UT. Then after the end of the main phase Dst index returns to its quiet condition. These stage is the recovery phase of the storm. On the recovery phase Bz turns south north flactuation. Non-significant ionospheric response observed at all station except aboo, during the recovery phase.

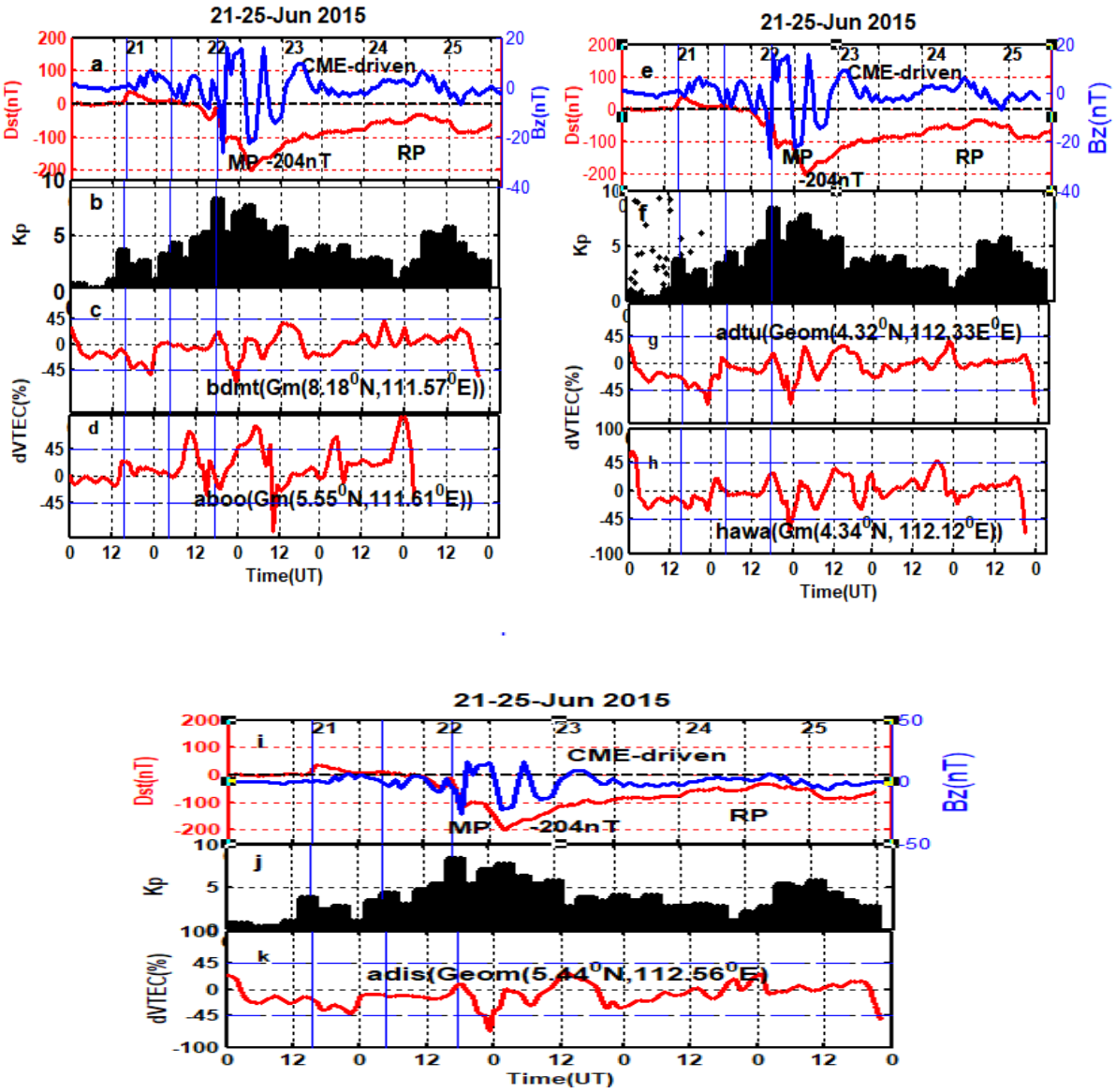

Figure 4.13: Dst and Bz top, kp upper- middle, and ionospheric deviation lower-middle, and bottom panel of 21-25 jun 2015. The solid blue vertical line is the onset time of the storm, Mp and Rp is the main and recovery phase of the storm. CME-Coronal mass ejection, SSC-Sudden storm commencment .

4.5.6 Geomagnetic activity of 30 Dec-3 January 2016

The variation of Dst , and Bz top panel, kp upper- middle panel, and ionospheric deviation lower-middle and bottom panel of 30 Dec-3 January 2016. The onset of the storm started on Decembere 30 at ∼00:50 UT. As shown in the Fig. 4.14 the main phase started on 31 of the same month. During the main phase Dst value depressed to the minimum value -110 nT with the corosponding kp value(kp=6). Bz turns south ward and atains a minimum value -14.5(nT) at ∼ 23:00UT. On the main phase the ionospheric deviation activity slightly enhanced at **hawa**, and **adis**(see, Fig 4.14, and non-significant at **bdmt**, **aboo**, and **adtu**.

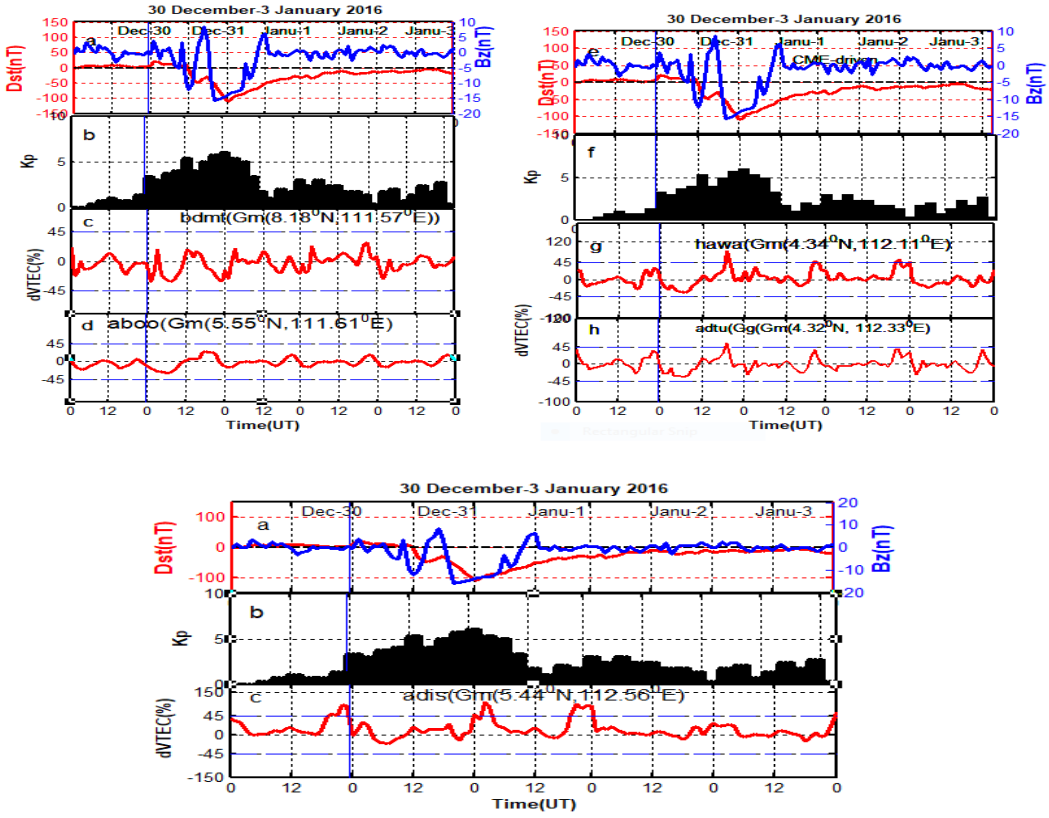

Figure 4.14: Dst, and Bz indice top panel, kp - middle panel, and ionospheric index activity (deviation) lower middle and and bottom panel of january 1,2015. Blue vertical line is the onset of the storm. Horizontal blue line plot is the upper and lower limit of non-significant ionospheric response.

When IMF interact with the earth magnetic field, it produce an electric field that penetrate from high latitude to mid-and low-latitude region due electro dynamo interaction. Positive ionospheric response observed in **hawa** and **aboo** during the night time is due to the effect of DDEF(Dugassa et al., 2020b).

4.5.7 Geomagnetic activity of 26-30 May 2017

Fig.4.15 the variation of ionospheric index activity with respect to Dst, Bz, and kp at **aboo**, **adtu**, and **adis** during the period of 26-30 May 2017. The SSC observed on day 27 at around 15:34 UT. During this time Bz turns south ward and attains a minimum value -19.5nT at 00:00 UT with kp=7, and its minimum Dst index is -125nT at 07:00 UT.

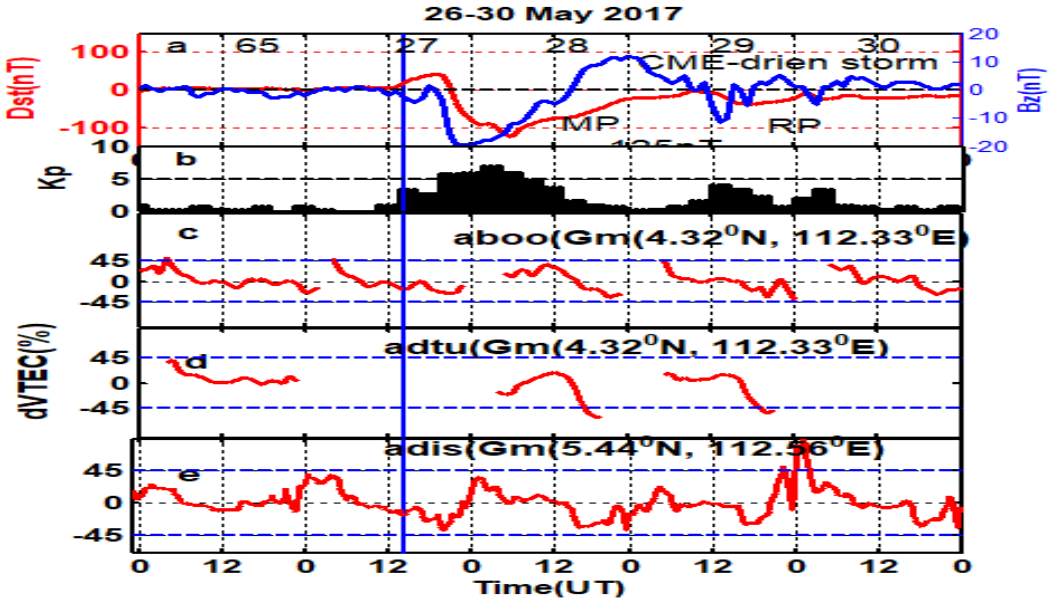

Figure 4.15: Dst and Bz top panel, kp upper-middle panel, ionospheric index activity ($\Delta VTEC$) at bdmt, aboo, and adis lower-middle, lower-lower -middle and bottom panel 26-30 May 2017. The solid blue vertical line is the onset of SSC, Mp and Rp is the main and recovery phase of the storm. SSC-sudden storm commencment, CME-Coronal mass ejection.

As shown in Fig .4.15 During the main phase there is a data gap at bdmt and adtu but non significant response at adis. The equivalent response during the recovery phase were non sig-

nificant at **bdmt**, slightly negative, at **adtu** and positive at **aboo** respectively. Out of thes the maximum positive ionospheric response observed at **adis** (89.22%) at around 1:00UT on 30 May 2017 before sun rise. There was no avaliable data to quantify ionospheric variability on bdmt and hawa during 26-30 May,2017.

Discussion

In this paper we analysed the response of F-region ionosphere effect that driven by CIR and CME geomagnetic storm over the selected GPS station and year. The characterstics of the ionized component of upper atmosphere during geomagnetic storms significantly deviates from the quiet day pattern of the ionosphere. The ionospheric TEC vary with respect to time, season, and geographic as well as geomagnetic location . Three CIR-driven geomagnetic storm with Dst <-88n, which occured during 5-9 january 2015, 18-22 january 2016 and 5-9 march 2016 and seven CME driven geomagnetic storms, that occurred during 15-19 march 2013, 30 Dec-3Jun 2013, 17-21 february 2014 , 15-19 March 2015, 21-25 jun 2015, 30 Dec-3Jun 2016, and 26-30 May 2017 that had been an avaliable TEC data was analized.

Significantly positive response observed in the evening-after midnight hours during the recovery phase of 5-9 january 2015, 18-22 january 2016 and 5-9 march 2016 and non significant response during the main phase of CIR driven storm (Sulungu and Uiso., 2019).Our result corelated with Chen et al. (2015) significant positive response of CIR diven storm occured during the night time of the recovery phase. The nighttime positive ionospheric storm effects could atributed due to the combined effects of the storm time thermospheric circulation, and DDEF which is eastward during the night period (Liu et al., 2015; Matamba and Habarulema., 2018). The positive ionospheric storms effect observed during the storm intial, main and recovery phase of 18-22 january 2016 at aruond the midd night. The basic mechanism for positive ionospheric response at low lattitude region are due to the avaliability of PPET, equatorward neutral winds, neutral composition changes by large-scale neutral wind circulation, and traveling atmospheric disturbances (Chen et al., 2015).

At low latitude the response of CME driven storm highly positive during the recovery phase at around the mid night, and more non significant during the main phase. Why becouse the ionospheric irregularity is greater at the pole and takes time to reached the equatore and the response should be observed during the recovery phase. The earth magnetic field is greater near to the pole

and decreased near to the equator (low lattitude). when Bz turns south ward more interaction (auroral) effect observed around the pole and moves to wards the equitor due to neutral wind circulation or travelling atmospheric disturbance. The response tooke time to reache the equitor (low latitude).

The ionospheric response of CME driven storm, gives a positive response during the main phase and recovery phase during the evening. During the evening the direction of PPEF in the equatorial region is west ward, and east ward during the day time. Positive response are more prolenedged during the main and recovery phase of CME driven storm. The ionospheric deviation driven by CME is more dominant as it compaired the ionospheric index activity driven by CIR. Because CME driven storm is more intense one , and moves with a very high speed to wards the interplanetary space ,and highly afect the electrone concentration as it compaired CIR driven.

Conclusion and Recommendation

4.6 Conclusion

The characteristics of the ionized component of upper atmosphere during geomagnetic storms significantly deviates from the quiet day pattern of the ionosphere. The deviation is commonly referred to as ionospheric storm. Geomagnetic storms can be driven by either CMEs, CIRs/HSSW, solar flare. In this study, we analysed the ionospheric responses to three CIR-driven geomagnetic storm with Dst<-88 nT that occured during 5-9 january 2015, 18-20 january 2016 and 5-9 march 2016 and CME driven geomagnetic storms which occurred during 15-19 march 2013, 30 May-3 jun 2013, 17-21 February 2014, 15-19 March 2015, 21-25 June 2015, 30 Dec-3 June 2016, and 26-30 May 2017 over the selected year and selected GPS station. UNAVCO GPS TEC data from bdmt, aboo, hawa, adis and adtu was used for this purpose. In the analysis GPS TEC data with elevation mask angle greater or equal to 20^0 was considered.

- Most of the ionospheric storm effects in the low latitude caused by the geomagnetic storms driven by CME, and CIR are Positive.
- Positive ionospheric response is more significante during the recovery phase and non significant response during the main phase for CIR driven storm.
- Because of weak magnetic field the area close to the equitor is more affected by geomagnetic storme as compaired than the area away from the equator.
- Positive response of CME drive storm highly observed during the main and recovery phase during the night time .
- Night time positive ionospheric response atributed due to DDEF,while day time is due to PPEF.

- The ionospheric index activity driven by CME is more significant as it compaired with CIR driven

Recommendation

Since this study is not covered the whole region of Ethiopia with long- term GPS observation data, ionospheric TEC variation studies from multi-GPS station with long-term observation is recommended.

ACKNOWLEDGEMENT

I would like to acknowledge Bahirdar university to give this free chance ,and NASAs Space Physics Data center Facility of OMNI Web interface site and UNVCO (University NAVSTAR Consortium http://www.unavco. org/data/gps-gnss/data/

References

Abdu, M. A. (1997). Major phenomena of the equatorial ionosphere-thermosphere system under disturbed conditions. Journal of Atmospheric and Solar-Terrestrial Physics, 59(13), 1505-1519.

Adeniyi, J. O., Doherty, P. H., Oladipo, O. A., Bolaji, O. (2014). Magnetic storm effects on the variation of TEC over Ilorin an equatorial station. 12451253. https://doi.org/10.1002/2014RS005404.Received

Athay, R. G. (2012). The solar chromosphere and corona: Quiet Sun (Vol. 53). Springer Science and Business Media.

Balan, N., Alleyne, H., Otsuka, Y., Lekshmi, D. V., Fejer, B. G., Mccrea, I., and Ox, D. (2009). Relative effect s of electric field and neutral wind on po s itive iono s pheric s torm s. 439445.

Balasis, G., Papadimitriou, C., and Boutsi, A. Z. (2019). Ionospheric response to solar and interplanetary disturbances: a Swarm perspective. Philosophical Transactions of the Royal Society A, 377(2148), 20180098.

Balogh, A., Gosling, J. T., Jokipii, J., Kallenbach, R., & Kunow, H. (Eds.). (1999). Corotating interaction regions (Vol. 7). Springer Science & Business Media.

Bittencourt, J. A. (2013). Fundamentals of plasma physics. Springer Science & Business Media.

Borovsky, J. E., and Denton, M. H. (2006). Differences between CME-driven storms and CIR-driven storms. Journal of Geophysical Research, 111, A07S08. https://doi.org/10.1029/2005JA011447

Borovsky, J. E., & Denton, M. H. (2006). Differences between CMEdriven storms and CIRdriven storms. Journal of Geophysical Research: Space Physics, 111(A7).

Brekke, A. (2013). Physics of the upper polar atmosphere. Springer Science & Business Media.

Bronarska, K., Michalek, G., Yashiro, S., & Akiyama, S. (2017). Visibility of coronal mass ejections in SOHO/LASCO coronagraphs. Advances in Space Research, 60(9), 2108-2115.

Buresova, D., et al. "Ionospheric disturbances under low solar activity conditions." Advances in Space Research 54.2 (2014): 185-196.

Candido, C. M., Batista, I. S., Klausner, V., de Siqueira Negreti, P. M., Becker-Guedes, F., de Paula, E. R..& Correia, E. S. (2018). Response of the total electron content at Brazilian low latitudes to corotating interaction region and high-speed streams during solar minimum 2008. Earth, Planets and Space, 70(1), 1-19.

Chakraborty, M., Kumar, S., De, B. K.,Guha, A. (2015). Effects of geomagnetic storm on low latitude ionospheric total electron content?: A case study from Indian sector. 5, 1115?1126.

Chen, Y., Wang, W., Burns, A. G., Liu, S., Gong, J., Yue, X.& Coster, A. (2015). Ionospheric response to CIRinduced recurrent geomagnetic activity during the declining phase of solar cycle 23. Journal of Geophysical Research: Space Physics, 120(2), 1394-1418.

Dugassa, T., Bosco, J., Nigussie, M. (2020a). Statistical study of geomagnetic storm effects on the occurrence of ionospheric irregularities over equatorial / low-latitude region of Africa from 2001 to 2017. Journal of Atmospheric and Solar-Terrestrial Physics, 199(December 2019), 105198. https://doi.org/10.1016/j.jastp.2020.105198

Dugassa, T., Bosco, J., Nigussie, M. (2020).Equatorial and low-latitude ionospheric TEC response to CIR-driven geomagnetic storms at different longitude sectors. Advances in Space Research, 66(8), 1947?1966. https://doi.org/10.1016/j.asr.2020.07.003

Fagundes, P. R., Cardoso, F. A., Fejer, B. G., Venkatesh, K., Ribeiro, B. A. G., & Pillat, V. G. (2016). Positive and negative GPSTEC ionospheric storm effects during the extreme space weather event of March 2015 over the Brazilian sector. Journal of Geophysical Research: Space Physics, 121(6), 5613-5625.

Farid, H. M., Mawad, R., Ghamry, E Yoshikawa, A. (2020). The Impact of Coronal Mass Ejections on the Seasonal Variation of the Ionospheric Critical Frequency f0F2. Universe, 6(11), 200.

Gonzalez, W. D., Joselyn, J. A., Kamide, Y., Kroehl, H. W., Rostoker, G., Tsurutani, B. T.,& Vasyliunas, V. M. (1994). What is a geomagnetic storm?. Journal of Geophysical Research: Space Physics, 99(A4), 5771-5792.

Guarnieri, F. L., Tsurutani, B. T., Gonzalez, W. D., Echer, E., Gonzalez, A. L., Grande, M., & Soraas, F. (2006, February). ICME and CIR storms with particular emphasis on HILDCAA events. In ILWS Workshop (pp. 19-20).

Hutchinson, J. A., Wright, D. M., Milan, S. E., Grocott, A., Physics, S. P. (2011). 42nd Lunar and Planetary Science Conference (2011) 42nd Lunar and Planetary Science Conference (2011).45.

Huttunen, K. E. J., Koskinen, H. E., & Schwenn, R. (2002). Variability of magnetospheric storms driven by different solar wind perturbations. Journal of Geophysical Research: Space Physics, 107(A7), SMP-20.

Jin, S., and Jin, R. (2017). Positive and negative ionospheric responses to the March 2015 geomagnetic storm from BDS observations. Journal of Geodesy, 91(6), 613626. https://doi.org/10.1007/s00190-016-0988-4

Kassa, T., Damtie, B., and Yizengaw, E. (2012). The Response of Ethiopian Ionosphere to the Magnetic Storm of 11 October 2008. October 2008, 15.

Kassa, T., Damtie, B., & Yizengaw, E. (2012). The Response of Ethiopian Ionosphere to the Magnetic Storm of 11 October 2008. Lat. Am. J. Phys. Educ. Vol, 6(2), 322.

Kelley, M. C. (2013). The Earth s Ionosphere Second Edition.

Krishna, G. (2017). GPS-TEC analysis application. 19.

Kugblenu, S., Taguchi, S.Okuzawa, T. (1999). Prediction of the geomagnetic storm associated Dst index using an artificial neural network algorithm. 307313.

Lamarque, J. F., and P. Hess. "STRATOSPHERE/TROPOSPHERE EXCHANGE and STRUCTURE— Local Processes." (2015): 262-268.

Meseret, L. (2019). STUDYING THE VARIABILITY OF THE IONOSPHERE USING SUPERSID MONITOR AND SWARM SATELLITE DATA (Doctoral dissertation).

Liu, G., Huang, W., Shen, H., Aa, E., Li, M., Liu, S., & Luo, B. (2019). Ionospheric response to the 2018 sudden stratospheric warming event at middleand lowlatitude stations over China sector. Space Weather, 17(8), 1230-1240.

Lissa, D., Srinivasu, V. K. D., Prasad, D. S. V. V. D., & Niranjan, K. (2020). Ionospheric response to the 26 August 2018 geomagnetic storm using GPS-TEC observations along 80 E and 120 E longitudes in the Asian sector. Advances in Space Research, 66(6), 1427-1440.

Liu, Y., Fu, L., Wang, J., Zhang, C. (2018). Studying Ionosphere Responses to a Geomagnetic Storm in June 2015 with Multi-Constellation Observations. June 2015, 120. https://doi.org/10.3390/rs10050666

Livingston, W., & Penn, M. (2009). Are sunspots different during this solar minimum?. Eos, Transactions American Geophysical Union, 90(30), 257-258.

Imada, S., Matoba, K., Fujiyama, M.,Iijima, H. (2020). Solar cycle related variation in solar differential rotation and meridional flow in solar cycle 24. Earth, Planets and Space. https://doi.org/10.1186/s40623-020-01314

Markovi, M. (2015). Determination of total electron content in the ionosphere using GPS technology. Geonauka, 02(04), 19. https://doi.org/10.14438/gn.2014.22

Matamba, T. M., Habarulema, J. B. (2018). Ionospheric Responses to CME- and CIR-Driven Geomagnetic Storms Along 30^0E - 40^0E Over the African Sector From 2001 to 2015. 538556. https://doi.org/10.1029/2017SW001754

Matamba, T. M., Habarulema, J. B. Mckinnell, L.(2015). Statistical analysis of the ionospheric response during geomagnetic storm conditions over South Africa using ionosonde and GPS data. November 2004, 536547. https://doi.org/10.1002/2015SW001218.

Msganaw, A., Abraha, G., Kassa, T. (2019). Solar Activity and Geomagnetic Storm Effects on GPS Ionospheric TEC over. 11(2), 276300

Nigussie, M. (2013). Formation of ionosphere. Unpublished space one notes

Oryema, B., Jurua, E., Dujanga, F. M., & Ssebiyonga, N. (2015). Investigation of TEC variations over the magnetic equatorial and equatorial anomaly regions of the African sector. Advances in Space Research, 56(9), 1939-1950.

Pande, B., Mathpal, M. C.&Pande, S. (2017). Statistical Analysis of Geomagnetic Activity and Solar Activity Features during Solar Cycle 23 & 24. 6(2), 1420.

Patel, K., Singh, A., Singh, S. B., & Singh, A. K. (2019). Causes responsible for intense and severe storms during the declining phase of Solar Cycle 24. Journal of Astrophysics and Astronomy, 40(1), 4.

Pokhotelov, D., Jayachandran, P. T., Mitchell, C. N., & Denton, M. H. (2010). High-latitude ionospheric response to co-rotating interaction region-and coronal mass ejection-driven geomagnetic storms revealed by GPS tomography and ionosondes. Proceedings of the Royal Society A: Mathematical, Physical and Engineering Sciences, 466(2123), 3391-3408.

Prölss, G. W. (1993). Common origin of positive ionospheric storms at middle latitudes and the geomagnetic activity effect at low latitudes. Journal of Geophysical Research: Space Physics, 98(A4), 5981-5991.

Purohit, P. K., Mansoori, A. A., Khan, P. A., Atulkar, R., Bhawre, P., Tripathi, S. C. & Gwal, A. K. (2015, September). Evaluation of geomagnetic storm effects on the GPS derived Total Electron Content (TEC). In Journal of Physics: Conference Series (Vol. 640, No. 1, p. 012072). IOP Publishing.

Qui., Yan-Hong, C., Wen-Bin, W., Jian-Cun, G., & Si-Qing, L. (2015). Statistical analysis of the ionosphere response to the CIR and CME in Mid-latitude regions. Chinese Journal of Geophysics, 58(7), 2250-2262.

Ratnam, D. V., Sivavaraprasad, G., Devi, N. S. M. P. L. (2016). Analysis of Ionosphere Variability over Low-latitude GNSS Stations during 24th Solar Maximum Period. Advances in Space Research. https://doi.org/10.1016/j.asr.2016.08.041

Revallo, Milo, et al. (2015). "Modeling of CME and CIR driven geomagnetic storms by means of artificial neural networks." Contributions to Geophysics and Geodesy 45.1, 53-65.

Richardson, Ian G., and Hilary V. Cane. "Near-Earth interplanetary coronal mass ejections during solar cycle 23 (19962009): Catalog and summary of properties." Solar Physics 264.1 (2010): 189-237.

Rishbeth, H. (2015). Evaluation of geomagnetic storm effects on the GPS derived Total Electron Content (TEC) Evaluation of geomagnetic storm effects on the GPS derived Total Electron Content (TEC). https://doi.org/10.1088/1742-6596/640/1/012072

Schillings, A. (2017).Licentiate thesis O + outflow during geomagnetic storms observed by Cluster satellites. An- Nales Geophysicae, 35, 13411352.

Shim, J. S. (2009). DigitalCommons USU Analysis of Total Electron Content (TEC) Variations in the Low- and Middle-Latitude Ionosphere

Sulungu, E. D., Uiso, C. (2019). Ionospheric TEC Response to Geomagnetic Storms Occurred on 15-20 March 2013 and 2015 over the Eastern Africa Region. 3(4), 103111. https://doi.org/10.11648/j.ajese.20190304.16

Tariq, M. A., Shah, M.,Iqbal, M. H. T. (2019). Ionospheric VTEC variations over Pakistan in the descending phase of solar activity during 2016 17. Astrophys Space Sci. https://doi.org/10.1007/s10509-019-3591-3

Twinomugisha, F., Ssebiyonga, N., Florence, M. D. (2017). TEC derived from some GPS stations in East African equatorial region and comparison with the TEC from NeQuick2 model. Advances in Space Research, 60(9), 1905?1920. https://doi.org/10.1016/j.asr.2017.07.018 Variations in the Low- and Middle-Latitude Ionosphere

van der Merwe, S. J., Pierre Cilliers, and Pieter de Villiers. "Characterization of the Ionosphere over the South Atlantic Anomaly by using a ship based Dual Frequency GPS receiver as aid for HF propagation path prediction."

Vijaya Lekshmi, D., Balan, N., Tulasi Ram, S., Liu, J. Y. (2011). Statistics of geomagnetic storms and ionospheric storms at low and mid latitudes in two solar cycles. Journal of Geophysical Research: Space Physics, 116(11), 113. https://doi.org/10.1029/2011JA017042

Wyllie, J. S.(2007). Modeling The Temporal Variation Of The Ionosphere.

Yaacob, N., Abdullah, M.,and Ismail, M. (2010). GPS total electron content (TEC) prediction at ionosphere layer over the equatorial region. Trends in Telecommunications Technologies.

Yokoyama, N, and Y Kamide. 1997. Statistical Nature of Geomagnetic Storms. 102.

Declaration

I hereby declare that this thesis is my original work and has not been presented for a degree in any other university, and that all sources of material have been duly aknowledged.

Name: **Chernet Wubet**

Signature:_____

Date:July, 2021

this thesis has been submited for examination with my approval as university advisor.

Name: Ambelu Tebabal (PhD)

Signature:_____

Date:July, 2021